

## Research Article

# Study on the Process and Mechanism of Slope Failure Induced by Mining under Open Pit Slope: A Case Study from Yanqianshan Iron Mine, China

Yingpeng Hu , Fengyu Ren, Hangxing Ding , Yu Fu, and Baohui Tan 

*School of Resources and Civil Engineering, Northeastern University, Shenyang 110819, China*

Correspondence should be addressed to Hangxing Ding; [dinghangxing@mail.neu.edu.cn](mailto:dinghangxing@mail.neu.edu.cn)

Received 30 October 2018; Revised 18 January 2019; Accepted 4 February 2019; Published 6 March 2019

Academic Editor: Jian Ji

Copyright © 2019 Yingpeng Hu et al. This is an open access article distributed under the Creative Commons Attribution License, which permits unrestricted use, distribution, and reproduction in any medium, provided the original work is properly cited.

Mining under an open pit slope results in the collapse and slide of the slope. In this paper, a combination of methods including Google Earth and field investigations is applied to investigate the process of eastern slope failure induced by underground mining in the Yanqianshan Iron Mine over five years. According to the observed ground deformation features, the geomorphic zone of the eastern slope can be divided into four regions (caved rock zone, cracking zone, toppling zone, and sliding zone). Break angles and fracture initiation angles at different times are counted separately. Based on the above work, the process of initiation and development of slope failure is studied. The analysis results show that the process of slope failure could be chronologically divided into three stages. First, a collapse pit, caused by the falling of the overlying strata above the goaf, appeared on the eastern slope. Then, the rock mass around the collapse pit slid into the pit to form a small landslide. Finally, because of mining disturbances and rock creep, a large landslide occurred on the northeastern phyllite slope. The control mechanisms of each failure stage are discussed separately. Finally, the RFP3D code is employed to simulate the slope failure process under the influence of underground mining. The results are consistent with the field observations, which provided information on deformation failure and the mechanics of the slope that could not be directly observed in the field and deepened the mechanism analysis.

## 1. Introduction

In order to maximize mineral resource exploitation, the transition from open pit to underground mining is a feasible development for more open pit mines. During the transitional period, the residual orebody under the final slope should be exploited first. Mining under slopes will result in the movement and deformation of the rock stratum of pit slopes, which may further damage infrastructure and buildings on the surface. It not only threatens the safety of production but also endangers the environment. Therefore, increasing attention has been paid to research on the process and mechanism of slope failure caused by underground mining.

Even to this day, surface deformation caused by underground mining is still one of the most challenging

problems in mining engineering. Research on coal mining subsidence prediction has been performed for nearly two hundred years. According to a large number of measurements of mining subsidence, empirical formulas, curves, graphs, and influence functions [1,2] have been developed. However, most empirical and analytical methods for predicting subsidence are only effective for simple geometries, which are generally inadequate for complex surface geometries.

Compared with coal mining, the shape and occurrence of a metal orebody are more complex, so the geometric configuration of the mining-out area changes rapidly. Meanwhile, the geological structure of metal mines is more complex, and the surface movement is significantly restricted by geological features such as faults and joints [3].

The above studies mainly focus on mining under relatively flat surfaces. There are limited cases in which mining under hillsides or slopes can trigger stratum collapses and landslides in these specific areas [4–6].

Advances in ground deformation monitoring contribute to the study of ground deformation. In recent decades, remote sensing technologies that have been successfully applied to surface monitoring include LiDAR laser scanning [7, 8], photogrammetry [9], and differential interferometric synthetic aperture radar (DInSAR) [10–12].

Combining historical aerial photographs with digital photogrammetric modeling and point cloud analysis techniques as well as geomorphological mapping, Clayton et al. [13] studied the failure process and mechanism of the Mitchell Creek Landslide (MCL) in northern British Columbia.

Compared with the expensive and sophisticated monitoring techniques described above, Google Earth offers a more accessible way to observe surface damage by providing free three-dimensional high-resolution satellite images [14–16].

In contrast to the expensive high-tech observation methods, field investigation has the defect of low measurement accuracy, but long-term field investigation and records of the surface failure characteristics remain valuable data for studying surface collapse. According to long-term periodic mapping of ground cracks at the Kiirunavaara Mine, Villegas et al. summarized three different stages of surface deformation [17].

A numerical simulation can effectively analyze the stresses, strains, and displacement distributions of rock in the mining process. Some researchers have used numerical simulation methods based on continuous medium mechanics, such as the finite element method (FEM) and finite difference method (FDM), to study the movement and failure modes of strata and surfaces caused by underground mining [18–26].

However, different from conventional underground excavation [27], the mechanical behavior of strata in response to underground mining is very complex. On the one hand, roof caving and surface collapse caused by underground mining turn complete rock masses into loose blocks; therefore, the mechanical properties of rock masses before and after collapse are significantly different [28–30]. Underground mining often leads to large deformations, discontinuous movements, and failure of the ground. Numerical simulation methods that rely on grids, such as FEMs and FDMs, will encounter the problem of grid deformation. These issues hinder the application of continuous medium numerical simulation in the study of surface failure caused by caving mining.

The distinct element method (DEM) has the intrinsic ability to simulate the discontinuous and large displacement of rock masses. Some researchers have used UDEC software, used to apply the DEM, to simulate roof failure and collapse during underground coal mining [31–34]. Salmi et al. studied a coal mining-induced landslide in Nattai North, Australia, using the DEM-based software UDEC [6]. Svartsjaern et al. utilized the DEM-based

software PFC2D to simulate footwall rock mass damage induced by sublevel caving at the Kiirunavaara Mine [35]. Using the DEM-based software 3DEC, Xu et al. simulated the influence of underground mining at the Yanqianshan Iron Mine on the eastern slope and predicted the damage range on the slope [36]. However, when DEM is used to carry out numerical simulation, if the number of blocks in the model is too large, the computational efficiency will be very low. Meanwhile, there is a risk that the calculation results will not converge.

In addition, some researchers have used a finite element/discrete element approach to simulate the influence of large-scale underground mining on the failure of open slopes [29].

RFPA3D is a numerical software package that can simulate completely progressive failure and macroscopic mechanical behavior of rock materials. Readers are referred to more detailed information about the RFPA2D model by Li et al. [37–39]. Liang et al. developed the 2D numerical code (RFPA2D) into a 3D code (RFPA3D) to investigate complex fracture growth in three dimensions [40].

In recent years, RFPA3D has been successfully applied to the mechanical analysis of engineering cases. Xu et al. used the creep calculation method of RFPA3D to study the mechanism of the Jiweishan landslide in the Sichuan province, China [41]. Zhang et al. explored the mechanism of the southern slope landslide of the Fushun West Open pit coal mine in China [42].

Based on Google Earth satellite photos and records of in-site surface failure characteristics of the eastern slope in the Yanqianshan Iron Mine for more than four years, this paper analyzes the overall process of slope failure caused by underground mining, illustrates the failure mechanism, and finally simulates the failure process using RFPA3D code.

## 2. Geological Settings

The Yanqianshan Iron Mine, which was first constructed in 1960, is located in Anshan city, Liaoning Province, China. The open pit mining was finished in September 2012. After more than half a century of mining, a huge open pit had formed, which was 1400 m long from east to west and 600 m to 700 m wide from north to south. The elevation of the closed loop of the pit is approximately 90 m and that of the ultimate bottom is –183 m. The southern, northern, western, and eastern slope angles are approximately 35° to 38°, 32° to 35°, 30°, and 43°, respectively.

The research area is located on the eastern slope of the Yanqianshan open pit, as shown in the red box in Figure 1. In this area, the main iron orebody is located in the middle, strikes about east-west, dips to the northeast at approximately 70–88°, and has a width from 60 m to 200 m in the south-north direction. Carbonaceous phyllite and diorite are exposed in the north of the research area. There are fragmented structures and strongly weathered zones in the carbonaceous phyllite. Diorite is on the northwestern part of the phyllite, and a faulted contact is found between the carbonaceous phyllite and the diorite. A wall-like branched

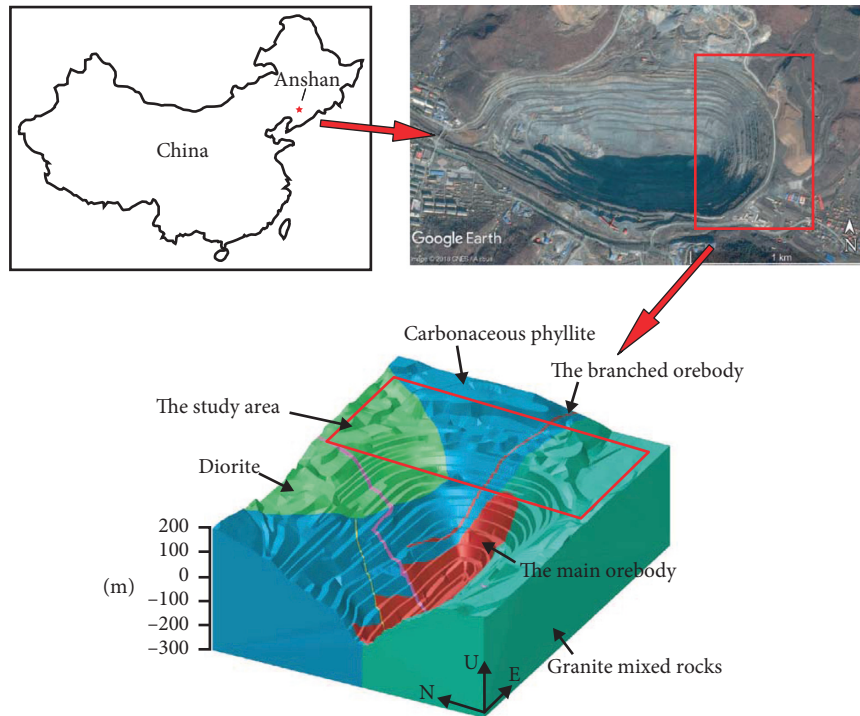


FIGURE 1: The location and geological model of the Yanqianshan Iron Mine.

orebody, paralleling the strike of the main orebody, is inserted in the phyllite. The southern region of the study area is mainly distributed with granite mixed rocks. There are three dominant groups of joints in each type of rock mass in the study area. The distributions of those three dominant sets of joints are quite similar in terms of occurrence, so there are three main sets of joints that can represent the structural surface distribution of the entire study area. The average orientations and dip angles of the three dominant sets of joints are  $40^\circ \angle 75^\circ$ ,  $220^\circ \angle 20^\circ$ , and  $300^\circ \angle 80^\circ$ , respectively [36].

After the end of open pit mining, the residual orebody under the eastern final slope began to be exploited. A sublevel caving method (Figure 2(a)), with horizontal slice mining from top to bottom, was employed. The orebody beneath the eastern slope is divided from top to bottom into five horizontal layers: the elevation ranges for the first to the fifth layer are  $-51$  m to  $-69$  m,  $-69$  m to  $-87$  m,  $-87$  m to  $-105$  m,  $-105$  m to  $-123$  m, and  $-123$  m to  $-141$ , respectively (Figure 2(b)). The horizontal mining range of each layer is approximately 100 m to 220 m long from east to west and approximately 110 m to 130 m wide from south to north. The orebody is mined from the first to the fifth layer, and the mining direction for each layer is from east to west.

During the period from 2013 to 2017, underground mining was gradually promoted. By December 2017, the fifth layer had been mined. Continuous underground mining induced strata movement and caving, led to surface subsidence, and finally triggered landslides. The corresponding development state of underground mining and surface subsidence in each working period is described in detail in the next section.

### 3. Investigation and Analysis of the Geomorphological Evolution of the Eastern Slope Caused by Underground Mining

The field investigation and the Google Earth images are combined to identify and summarize the typical geomorphic deformation features. Detailed engineering geomorphological maps were made to record the surface deformation features on the eastern slope of the Yanqianshan Iron Mine for five years (2013–2017). It can make a fundamental contribution to further mechanism analysis.

*3.1. Classification of Surface Deformation Features.* Figure 3 shows a series of visible deformation features (including scarps, counterscarps, and open cracks) emerging on the eastern slope. Based on field investigations, a classification standard of typical morphological deformation features was defined (Table 1).

*3.2. Comprehensive Survey Method of the Geomorphological Evolution: Google Earth and Field Investigations.* Since the end of 2013, the surface of the eastern slope began to deform and generated a large number of cracks. The measurement of such cracks on-site represents a major challenge because of the large study area and varied topography. Thus, limited by labor costs and safety factors, it is very difficult to determine the morphology of the main cracks using only the artificial field measurements.

Google Earth (GE), launched by Google USA, provides a cost-effective and efficient way to survey surface

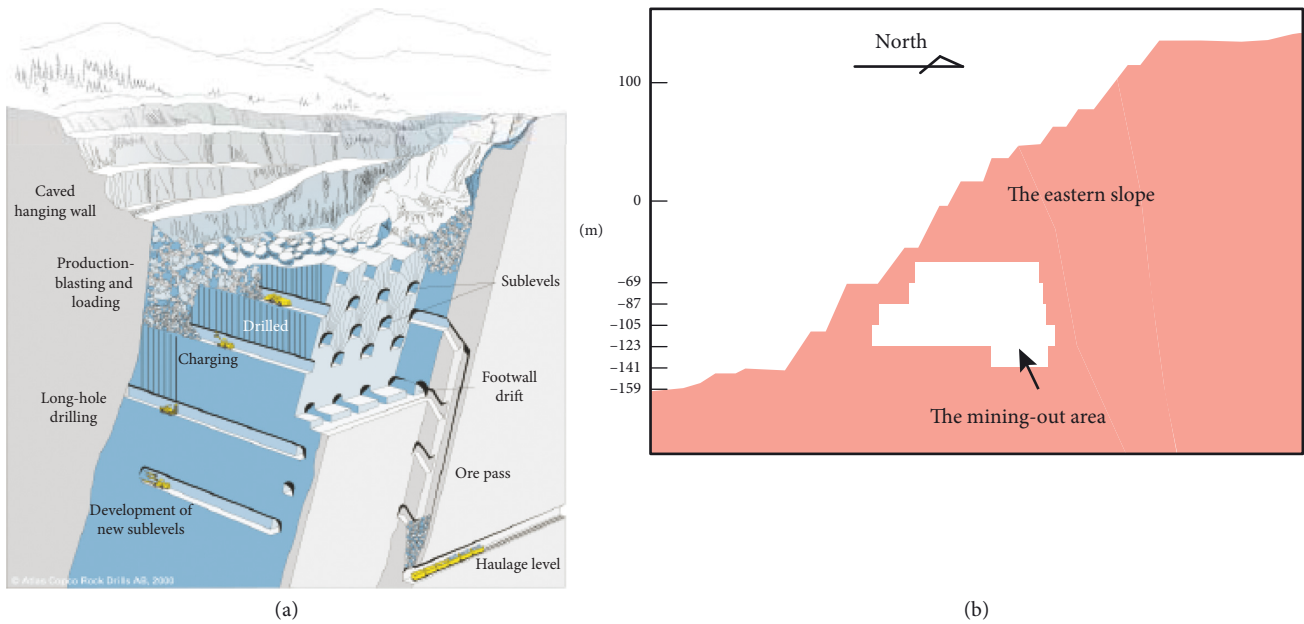


FIGURE 2: Illustration of (a) the typical sublevel caving method (image copyright: Atlas Copco) and (b) the sublevel caving under the slope.

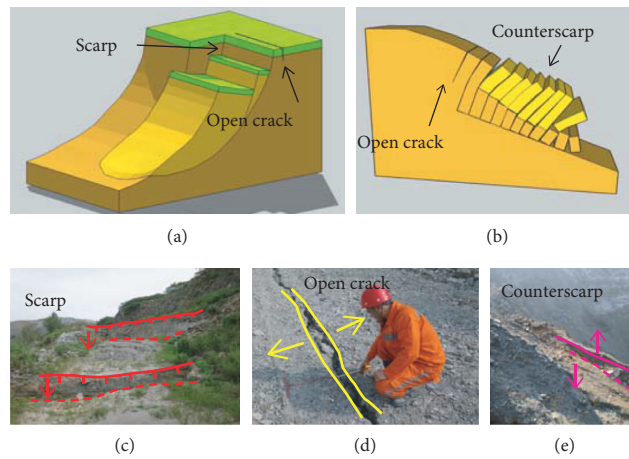


FIGURE 3: Illustration of the classification of surface deformation features.

TABLE 1: Description of the deformation feature classification.

Classification	Description
Open crack	Linear features within the landslide area Includes visible geologic structures Generally, caused by tensile stress
Scarp	Defines the boundary of the slide mass Normal movement indicator Obvious relative displacement caused by shear slip failure
Counterscarp	Antislope movement indicator Develops from open cracks Caused by toppling of the discrete rock blocks

deformation. GE is a virtual global tool that documents the Earth’s surface by integrating images from satellites, aerial photography, and geographic information systems (GISs) into a 3D global model.

Three advantages of GE enable its use to conduct long-term accurate and cost-free monitoring of geomorphological changes over a wide range of areas [43, 44].

- (1) GE offers high-resolution satellite photos for free, 46–60 cm per pixel, with excellent spatial resolution
- (2) GE provides multiple layers for users, among which the topographic map layer can use DEM data collected by NASA’s Space Shuttle Radar Topography Mission (SRTM) to observe topography at any angle in 3D space
- (3) GE has a time slider function, which adds a time-control function to the virtual earth view to provide satellite images of the same location at different times.

Because of the large extent of the open pit, the GE monitoring technique has its own advantages, as well as a number of shortcomings, as follows.

First, the poor weather in the area can affect the resolution of satellite images, resulting in faulty images. Second, although ground damage traces can be mapped by GE, the visible deformation features cannot be identified and classified reliably (scarps, counterscarps, or open cracks). Therefore, it is still necessary to combine the GE and field investigations in our study to document the progress of surface deformation with underground mining.

The process of surface deformation as determined by the combined approach is shown in Figure 4.

- (1) Since surface damage on the eastern slope caused by underground mining first appeared at the end of October 2013, the GE image taken in October 2012 was selected as the reference photo before the surface deformation. Take the surface deformation in October 2016 as an example. Based on the mark points and coordinates, the two GE images (2012-10 and 2016-10) were processed, and the plane images with the same area and the same proportion were output. After comparison, the surface deformation traces are identified and depicted in the treated plane image (2016-10).
- (2) We regularly conducted a field survey on the ground deformation features of the eastern slope at intervals of approximately 3-4 months. The main work includes locating the features by measuring the coordinates of a point on the trace with a portable GPS device, recording the trend and identifying the destruction type (scarps, counterscarps, and open cracks). After updating the GE satellite photos, a supplementary survey should be organized as soon as possible. According to the survey information before and after the satellite photos were taken and with the help of the virtual three-dimensional space provided by GE, the damage traces depicted on the satellite photos were reviewed to determine their accuracy and the types of the ground deformation features were identified and categorized (scarps, counterscarps, and open cracks). We found that the traces on the satellite photos could be verified by the surface survey, thereby demonstrating that the above-mentioned techniques can complement and verify each other.
- (3) According to the geomorphic deformation and underground mining in October 2016, the engineering geomorphological map illustrates the surface deformation caused by underground mining at the time.

Six GE images taken from 2013 to 2017 were selected to study the surface deformation process during underground mining. In this way, the geomorphological failures from 2013 to 2017 were plotted separately to study the evolution process of the surface deformation with the advance of mining.

*3.3. Investigation Results of Geomorphological Deformation.* In this section, based on GE images, field investigations, and the classification of geomorphological deformation,

engineering geomorphological maps, including surface failure features and the underground mining area, were plotted. The geomorphological change process of the slope caused by continuous underground mining is described.

*3.3.1. Investigation Results in November 2013.* The orebody under the eastern slope of the Yanqianshan Iron Mine began to be exploited in September 2012. By the beginning of November 2013, the  $-69$  m level had been mined. Then, a mined-out area, 136 m long in the east-west direction and 115 m wide in the south-north direction, was generated below the eastern slope (Figure 5(c)).

Despite the formation of the goaf, no subsidence was found on the eastern slope. Only one crack emerged along the western boundary of the horizontal projection of the goaf (Figure 5(b)). There were some rolling stones on the slope.

Based on Figure 5, the engineering geomorphological map on November 8, 2013, was drawn (Figure 6).

*3.3.2. Investigation Results in March 2014.* By the end of February 2014, the mining of the  $-69$  m level had been completed, and the  $-87$  m level was being mined. The goaf, 145 m long in the east-west direction and 120 m wide in the south-north direction, is shown in Figure 7(b).

On February 26, 2014, the first ground collapse on the eastern slope occurred (Figure 7(d)). The failure appeared on the transport highway at an elevation of 16 m, and the rock mass suddenly fell down to form a well-shaped collapse pit. Figure 7(a), taken on March 12, 2014, clearly shows the topographic destruction on the eastern slope after the initial surface collapse. It caused a small landslide of fragmented rock around the collapse pit to roll into the pit. A series of tension cracks appeared at the back of the landslide head scarp (Figure 7(c)), and others developed along the dominant joint set (average occurrence orientation/dip:  $317^{\circ}/41^{\circ}$ ). It is obvious that the discrete rock blocks separated from the original rock mass by cracks tend to slide towards the collapse pit.

According to Figure 7, the engineering geomorphological map on March 12, 2013, was drawn (Figure 8).

*3.3.3. Investigation Results in October 2015.* By the beginning of October 2015, the  $-69$  m and  $-87$  m levels had been mined out, and the mining of the  $-105$  m level had started. The horizontal projection of the mining area was 180 m long from east to west and 130 m wide from north to south (Figure 9(b)).

The survey results showed that, compared to March 2014, the range of the landslide increased significantly with the expansion of the collapse range (Figure 9). The head scarp of the small landslide developed up to  $+78$  m. Surrounding tensile failures occurred at the back of the head scarp. The northern boundary of the small landslide was defined by a side scarp trending in the east-west direction near the outcropped zone of the branched orebody. Some

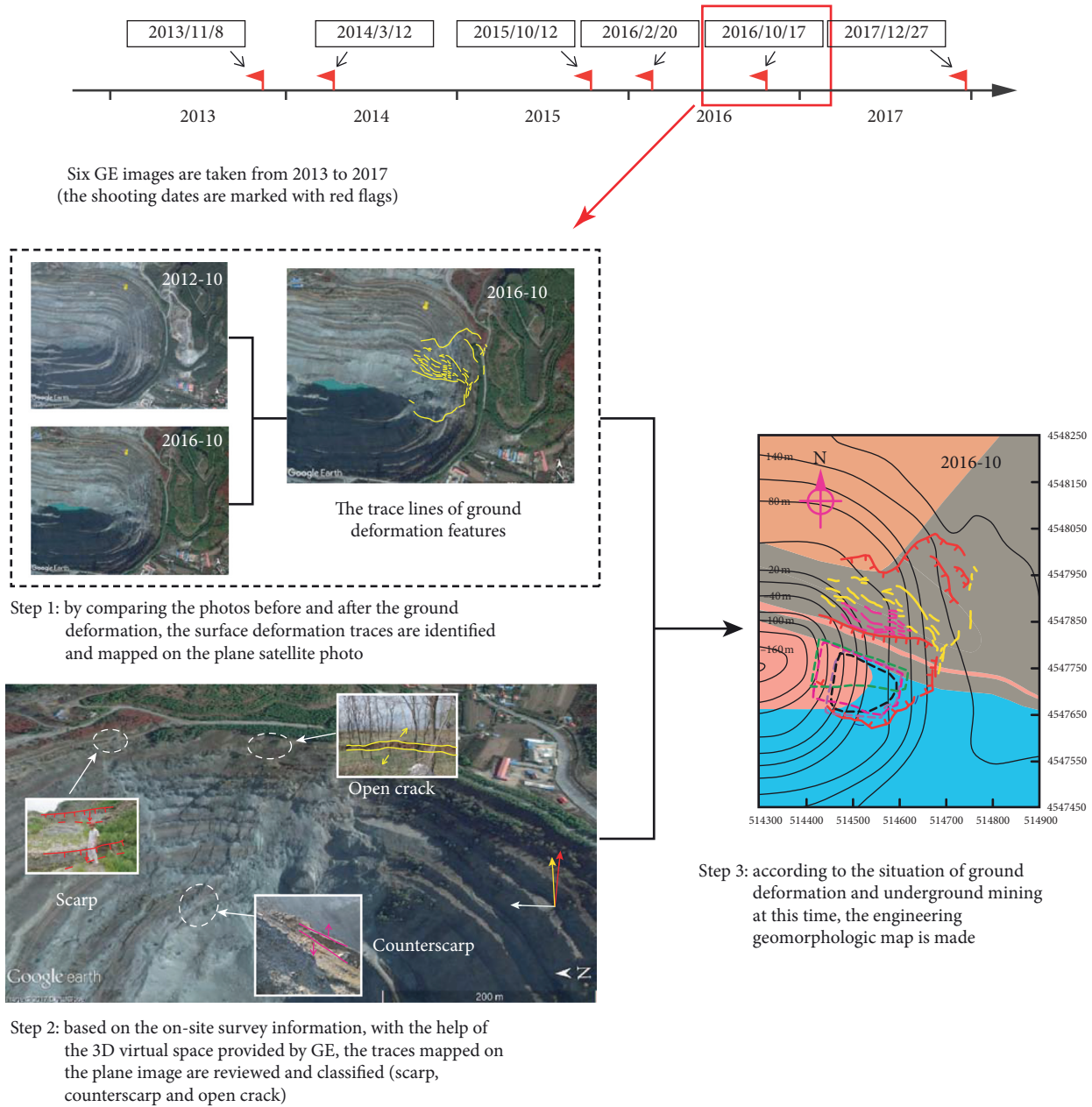


FIGURE 4: Illustration of the combined approach.

tensile cracks, ranging in length from 9 m to 20 m, were distributed behind the side scarp on the northern phyllite slope. The trending directions of these cracks were basically consistent with the trending direction of the dominant joint set (average occurrence orientation/dip:  $40^{\circ} \angle 75^{\circ}$ ). These cracks were controlled by the dominant structure planes. The side scarp defining the southern boundary of the small landslide was consistent with the horizontal projection of the southern boundary of the goaf. In contrast to the phyllite in north, the rock mass quality of granite mixed rocks on the southern slope is better. Only an 18 m long tensile crack was found at +36 m.

According to Figure 9, the engineering geomorphological map on October 12, 2015, was drawn (Figure 10).

3.3.4. Investigation Results in February 2016. By the end of February 2016, the -105 m and -123 m levels were in production. The horizontal plan of the mining area was 200 m long in the east-west direction and 130 m wide in the south-north direction (Figure 11(b)).

Compared with the previous period (October 2015), the Google Earth image (Figure 11(a)) of February 2016 shows that the range extension of the small landslide was limited. The landslide head scarp did not move upward, but the tension cracks in the rear of the scarp continued to develop. Existing cracks gradually penetrated, and new cracks were constantly produced. New tension cracks, also trending along the dominated joints (average occurrence orientation/dip:  $40^{\circ} \angle 75^{\circ}$ ), emerged on the northern phyllite slope. This

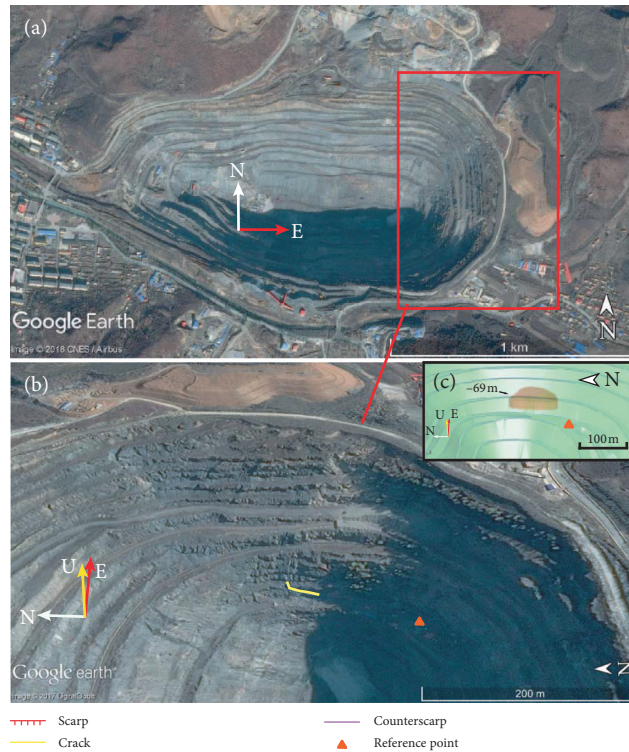


FIGURE 5: The survey of geomorphological changes on the eastern slope of the Yanqianshan Iron Mine (November 2013).

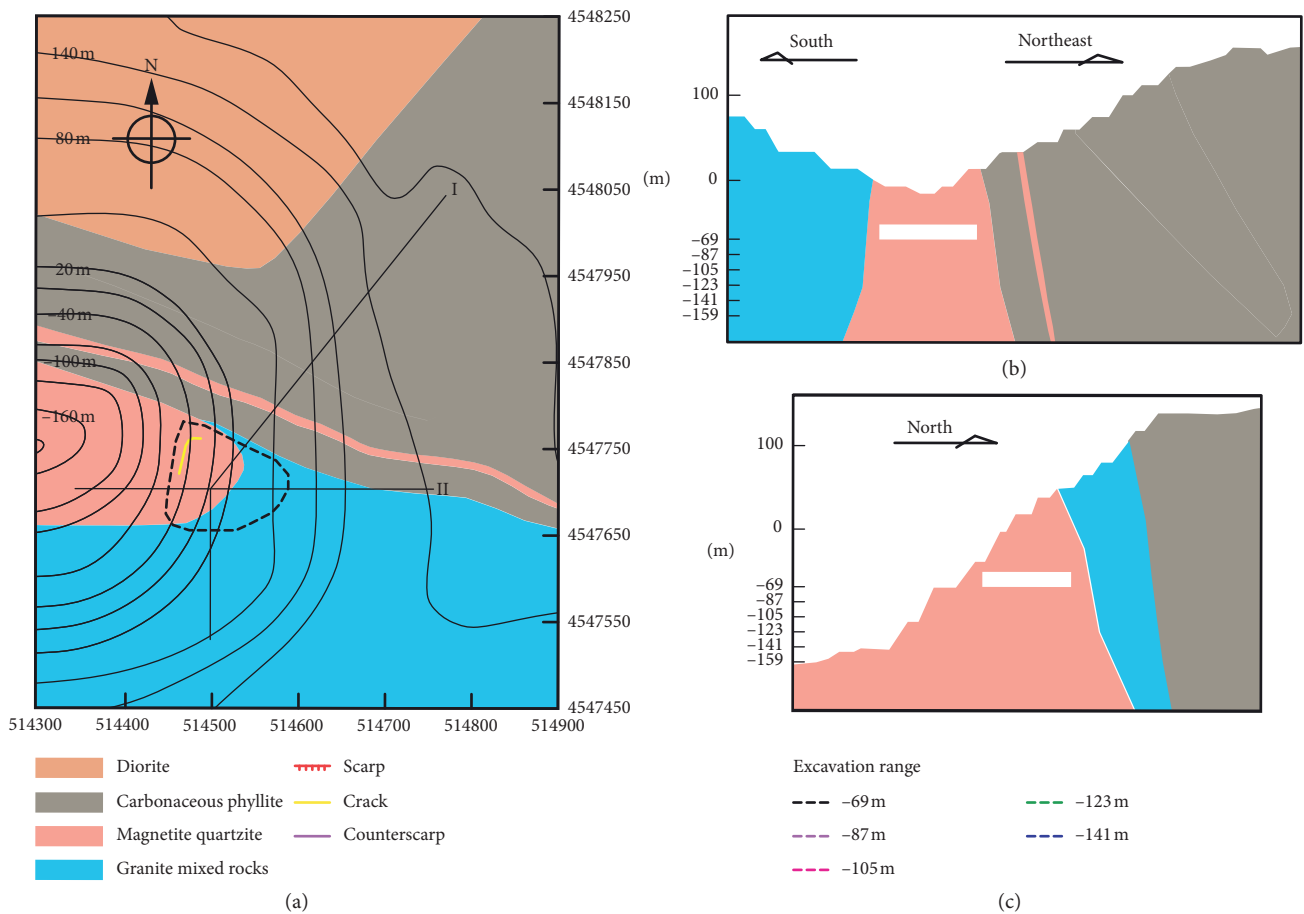


FIGURE 6: The engineering geomorphological map on November 8, 2013. (a) Distribution of ground destruction. (b) At profile I. (c) At profile II.



FIGURE 7: The survey of geomorphological changes on the eastern slope of the Yanqianshan Iron Mine (March 2014). (a) 3D view from Google Earth (12/3/2014). (b) The location of the mining area, which is observed through the same viewing angle as that of the Google Earth image (March 2014). (c) Tension cracks on the back of the small landslide head scarp. (d) The initial collapse pit (26/2/2014).

resulted in a northward extension of the distribution range of the cracks. The southern boundary of the small landslide did not change significantly. The previous fracture, located at +36 m, staggered and developed into a scarp. Interestingly, although the small landslide did not change significantly during the last four months, scarps caused by shear slip and open cracks produced by tensile failure appeared at the northeast edge of the open pit far away from the mining area (Figures 11(c)–11(e)).

According to Figure 10, the engineering geomorphological map on February 20, 2016, was plotted (Figure 12).

**3.3.5. Investigation Results in October 2016.** By October 2016, the  $-105$  m and  $-123$  m levels were being mined, and the horizontal projection of the mining area remained unchanged (Figure 13(b)).

After eight months of mining, Figure 13(a) shows that the geomorphology of the eastern slope had changed significantly. Tensile cracks behind the small landslide head scarp developed and connected with each other to separate rock mass, resulting in the head scarp rising up to +124 m. The location of the northern boundary of the small landslide did not change. However, with phyllite cut by the

cracks behind the northern side scarp bending and toppling downward into the collapse pit, the existing tensile cracks were transformed into counterscarps (Figure 13(c)). Simultaneously, new tension fissures were found in the rear of the counterscarps. The influence of the creep characteristics of phyllite on the eastern slope was fully revealed in the last eight months. Although the horizontal projection of the mining area did not change significantly during this period, a large landslide occurred on the northern phyllite slope. The new large landslide head crown, located at the northeast corner of the open pit, was identified by an arch-shaped scarp (Figure 13(d)) that developed from open cracks and slip failures (Figures 11(c)–11(e)) six months ago. The western boundary of the new large landslide was identified by an approximately 170 m long side scarp trending in the northeast-southwest direction. Coincidentally, the boundary coincided with the trace of the faulted contact between phyllites and diorites. The eastern boundary of the large landslide was made up of a series of discontinuous cracks that were 8–10 m long and trended along the dominated joints ( $300^{\circ}\angle 80^{\circ}$ ) (Figures 13(e) and 13(f)).

According to Figure 13, the engineering geomorphological map on October 17, 2016, was plotted (Figure 14).

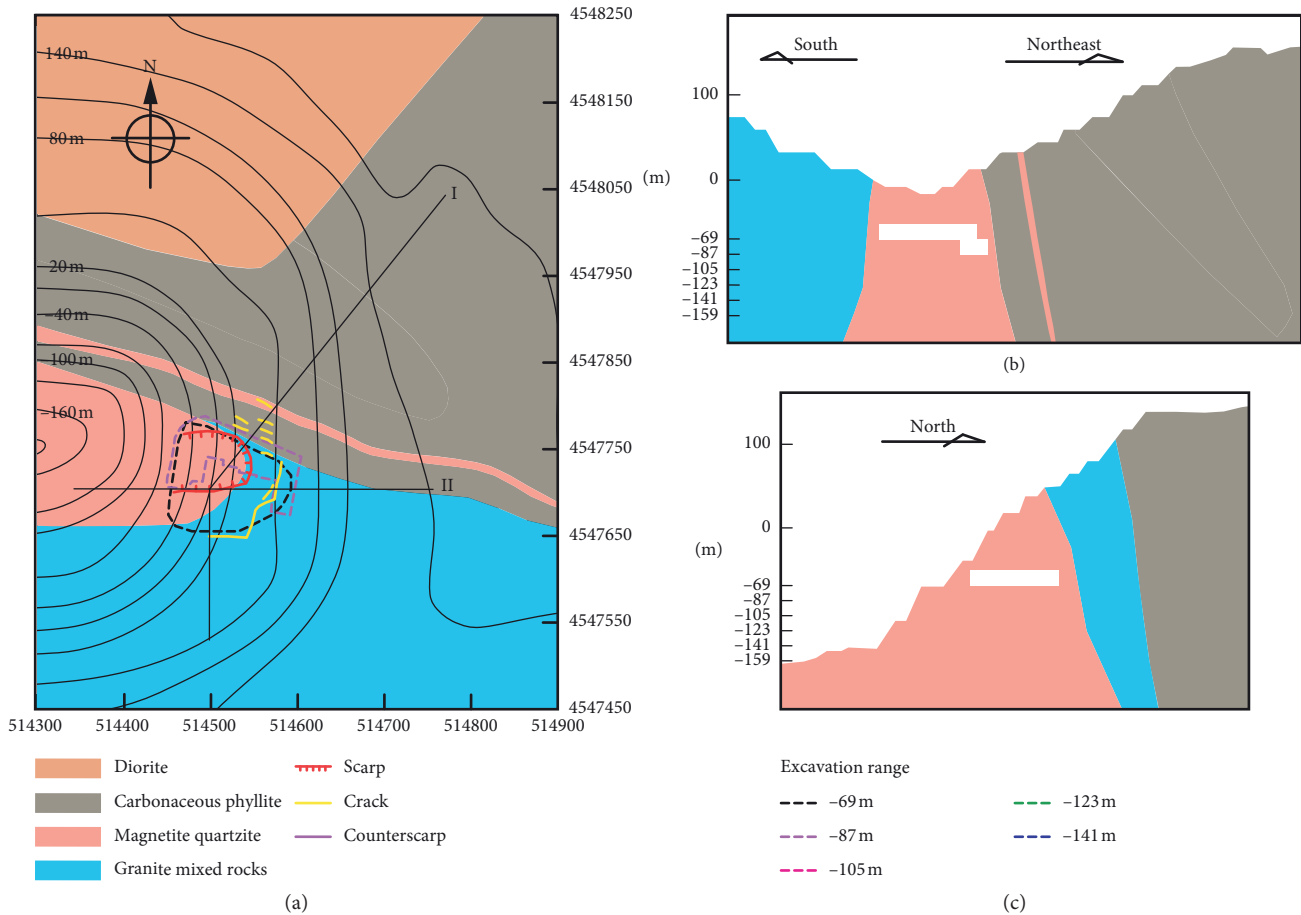


FIGURE 8: The engineering geomorphological map and mining progress on March 12, 2014. (a) Distribution of ground destruction. (b) At profile I. (c) At profile II.

3.3.6. Investigation Results in December 2017. By the end of 2017, the main orebody had been mined, including each orebody of the -51, -69, -87, -105, and -123 m levels, and the -141 m level was being mined. The horizontal projection of the mined-out area was approximately 220 m long in the east-west direction and approximately 132 m wide in the south-north direction (Figure 15(b)).

Figure 15(a) shows the further development of the new large landslide. The head scarp of the landslide was still located at +150 m in the northeast corner of the open pit. Discontinuous fractures along the eastern boundary developed into continuous scarps (Figures 15(e) and 15(f)), and the scarps were connected with the southern boundary of the old small landslide. Despite the lack of underground borehole data, strong evidence inferred the existence of a sliding surface below the northern phyllite slope because of the cracking (Figure 15(d)) and sliding near the head crown, shear failure along the eastern and western boundaries of the large landslide, and the main set of existing joints ( $220^{\circ}\angle 20^{\circ}$ ) (Figure 15(h)). It was clear that the sliding body of the large landslide began to slide southwestward. The sliding body still did not slip into the collapse pit at this time. However, many existing tensile cracks had developed into counterscarps, which can prove that the toppling failures of the phyllites

intensified under the squeezing action of the landslide body (Figures 15(c) and 15(g)).

According to Figure 15, the engineering geomorphological map on December 27, 2017, was plotted (Figure 16).

3.4. Summary. According to the distribution characteristics and change process of geomorphological destruction, the survey results are summarized as follows:

- (1) There are three main types of geomorphological failures on the slope: cracks, scarps, and counterscarps. The scarps caused by the collapse of the overlying rock strata above the goaf can indicate the boundary of the collapse pit. The scarps away from the goaf on the northeast corner of the open pit were produced by the rock mass sliding along the sliding surface. Most tension cracks and counterscarps occurred on the northern phyllite slope. They presented a type of continuous dynamic evolution. First, tensile cracks appeared along the dominant structure plane. Then, phyllite in the rear of the northern boundary of the small landslide was split into vertical layers by the cracks. The layered rock mass toppled down to the collapse pit, resulting in

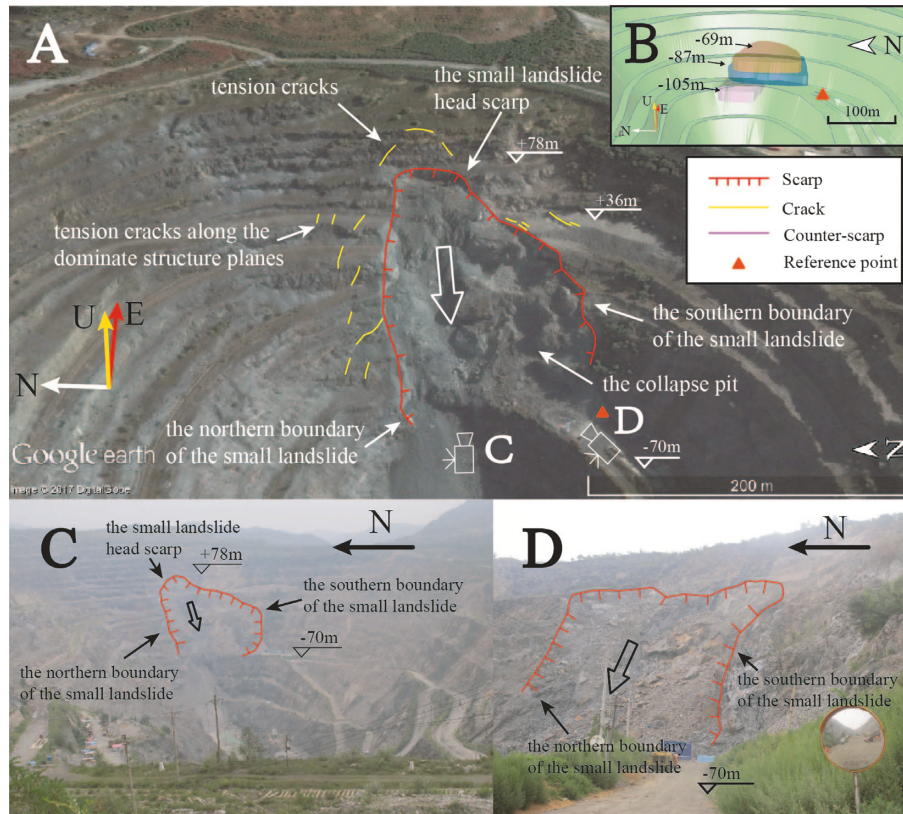


FIGURE 9: The survey of geomorphological changes of the eastern slope of the Yanqianshan Iron Mine (October 2015). (a) 3D view from Google Earth (12/10/2015). (b) The location of the mining area, which is observed through the same viewing angle as that of the Google Earth image (October 2015). (c) The small landslide on the eastern slope (east view). (d) The small landslide on the eastern slope.

tensile cracks developing into counterscarps. Simultaneously, new tension cracks occurred in the peripheral rock mass.

- (2) The distribution of the topographic failure features is not uniform. In the earlier stage of the eastern slope failure, the failure features appeared and a small landslide took place near the collapse pit. As the mining continued, most of the new deformation features appeared on the northern phyllite slope, where a new large landslide occurred.
- (3) The failure of the eastern slope can be divided into three stages. First, the surface subsidence induced by underground mining resulted in the collapse pit. Then, as the range of the collapse pit expanded, a small landslide gradually occurred around the pit. Finally, under the influence of underground mining disturbance and the creep deformation of phyllite, a large landslide, sliding southwestward, occurred on the northern phyllite slope.
- (4) The location and scope of the previous small landslide were controlled by the mined-out area. The location and scope of the later large landslide was controlled by the contact fault between the diorite and phyllite, the dominant joint sets, and the potential sliding surface.

**3.5. Surface Failure Zoning.** The surface failure caused by underground mining is generally considered to be divided into three regions: caved rock zone, fractured zone, and continuous subsidence zone (Figure 17) [45]. The angles between the lines connecting the boundary of the deepest mining area to the boundaries of the three regions and horizontal lines are, respectively, identified as the angle of break, angle of fracture initiation, and angle of subsidence. These data are powerful tools for studying the mechanics of surface failure caused by underground mining.

Because the time of occurrence and the range and extent of the eastern slope failure are difficult to predict, it is impossible to arrange a long-term observation network on the slope due to safety concerns. On the contrary, the remote monitoring methods of surface subsidence (such as DInSAR) are costly and complicated. Considering storage safety and cost, large-scale subsidence monitoring has not been carried out on the eastern slope. As a result, the continuous subsidence zone cannot be identified. However, the information from the caved rock zone and fractured zone can still be obtained through Google Earth images and field investigations, which can also provide sufficient information for the study of slope failure mechanism [17].

To further study the failure mechanism, the fractured zone of the eastern slope was further subdivided into three subregions (cracking zone, dumping zone, and sliding zone) based on the investigation results of the geomorphic

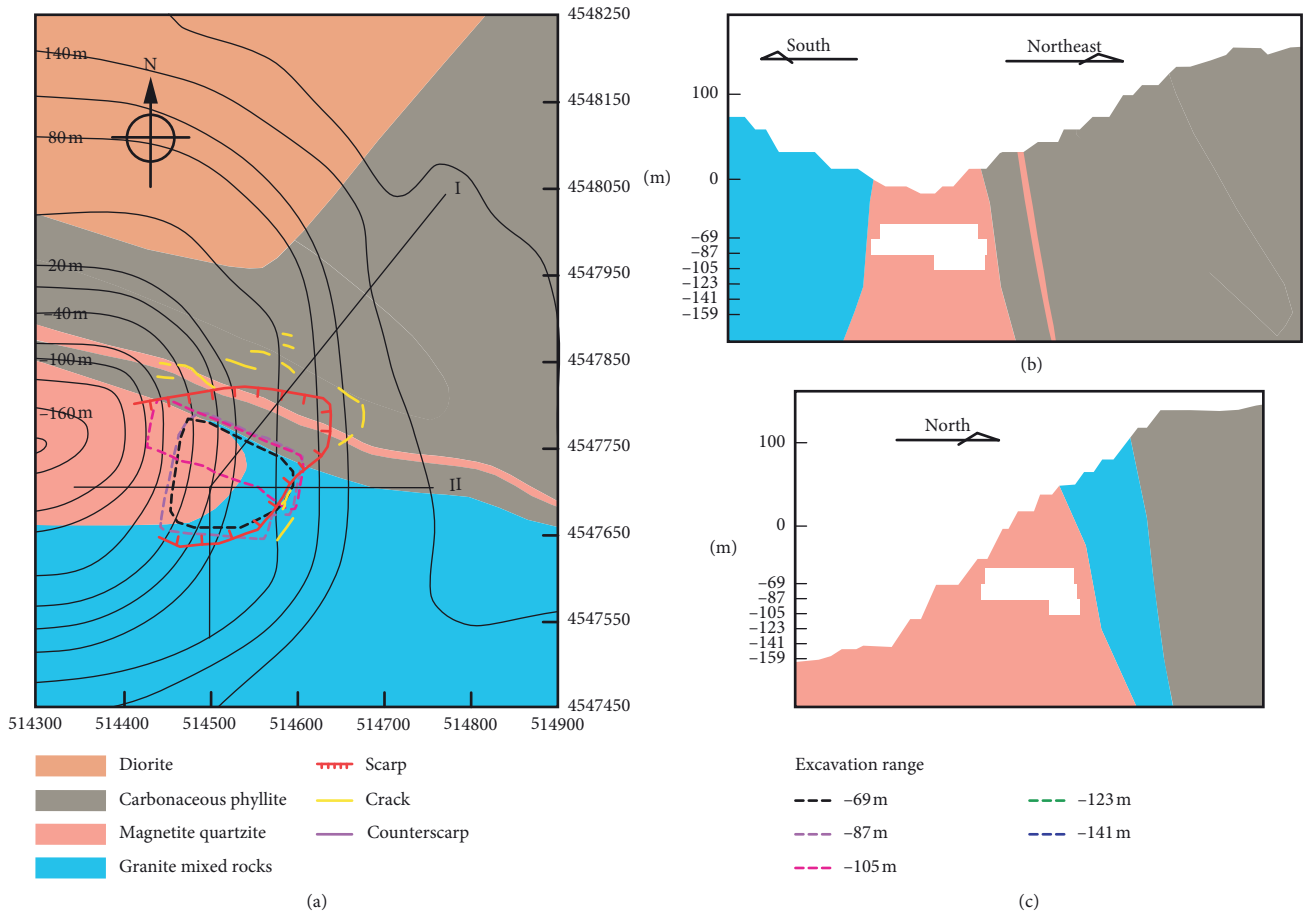


FIGURE 10: The engineering geomorphological map and mining progress on October 12, 2015. (a) Distribution of ground destruction. (b) At profile I. (c) At profile II.

destruction. Therefore, the destruction zone of the slope was divided into four regions:

- (a) *Caved Rock Zone*. Without the support below, the roof rock of the goaf falls down. Caving fracture propagates to the surface to form a collapse pit, and loose and fractured rocks fill the pit. Scarps around the pit can be marked as the range of the caved rock zone.
- (b) *Cracking Zone*. This area is located around the caved rock zone. The tensile failures characterized by open cracks are found in the region.
- (c) *Toppling Zone*. This region is characterized by counter cracks developed from tensile cracks. The existing cracks continually expand and converge to separate rock masses into discrete blocks, and the laminar rock blocks bend and topple. Finally, the open cracks develop into the counterscarps.
- (d) *Sliding Zone*. There are no obvious linear failure characteristics, such as fissures, in the region. However, shear slip deformations, such as scarps and cracks, occur along the edges of the region. The rock mass in the region presents an overall sliding tendency.

Based on the engineering geomorphological maps in different periods (Figures 6, 8, 10, 12, 14, and 16), the

variation of the surface failure partition on the eastern slope of the Yanqianshan Iron Mine is drawn to illustrate the failure process and explore the failure mechanism (Figure 18).

The underground mining area lies on the south side of the east-west axis of the eastern slope. In the early stage of mining, the failure range can also maintain north-south symmetry (Figure 18(b)). However, since the end of 2015, the failure area of the northern phyllite slope started to be larger than that of the southern granite mixed rock. By the end of 2017, the farthest distance from the east-west axis of the mining area to the boundary of the failure zone on the northern phyllite slope was approximately 320 m, which is much larger than approximately 90 m of the southern granite slope (Figure 18(f)). On the contrary, the surface failure mode of the northern phyllite slope was more complicated than that of the south, and all three subzones of the failure appeared and evolved on the northern slope.

In this case, although the angle of subsidence cannot be obtained due to the lack of displacement monitoring data, the failure mechanism can still be studied through the break angles and fracture initiation angles [17].

According to the two sections (profiles I and II) in Figure 18(a), the changes of the break angle (Figure 19) and

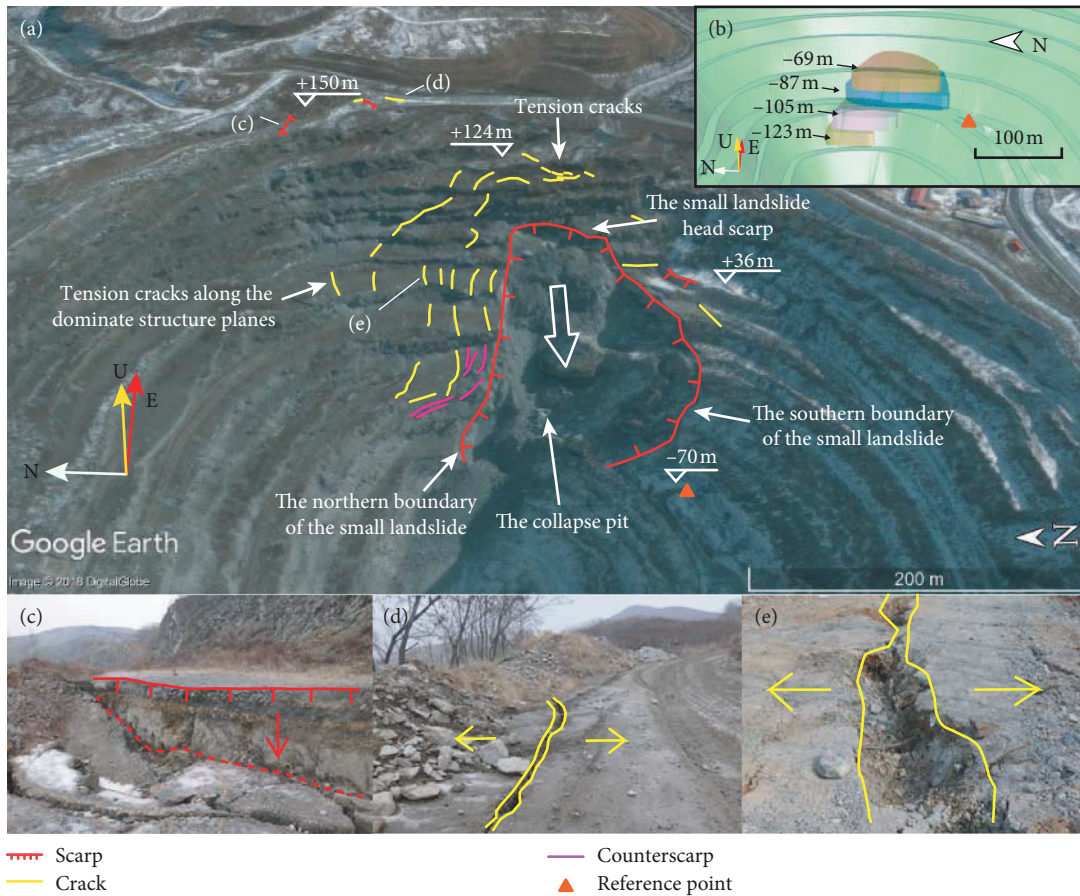


FIGURE 11: The survey of geomorphological changes of the eastern slope of the Yanqianshan Iron Mine (February 2016). (a) 3D view from Google Earth (20/2/2016). (b) The location of the mining area, which is observed through the same viewing angle as that of the Google Earth image (February 2016). (c) Scarp away from the small landslide. (d) Tension cracks away from the small landslide. (e) Tension cracks behind the side scarp (northern boundary) of the small landslide.

the fracture initiation angle (Figure 20) of five periods (2014-3, 2015-10, 2016-2, 2016-10, and 2017-12) were statistically analyzed (Figure 21).

The failure characteristics of granite mixed rock are similar to traditional surface collapse. After the collapse pit was formed, tension cracks appeared around the collapse pit. With the expansion and extension of the mining area, the break and fracture initiation angles increased accordingly.

Unlike the angle change rule in granite mixed rock, after dropping from 100 (March 2014) to 73 (February 2016), the break angle of the northern phyllite remained constant at 73 from February 2016 to December 2017. However, at the same time, the corresponding fracture initiation angle kept decreasing.

The following conclusions can be obtained according to the subdivision of the surface failure area and the break and fracture initiation angles:

- (1) Underground mining has the greatest impact on the northern phyllite slope, which eventually leads to a large landslide.
- (2) Before February 2016, the break angle is greater than  $90^\circ$ . The reason for this is that the stratum rock above the goaf is arched with a cantilever structure. The

stratum collapse process caused by underground mining is the progress of repeated failure and re-formation of the stress balance arch in the overburden strata from a mechanical point of view.

- (3) With the extension of the mining area, the fractured zone developed northward. However, the northward extension of the caved rock zone stopped near the wall-like branched orebody. It is different from the traditional mechanics of surface subsidence in which the caved rock zone and the fractured zone expand together. The branched orebody intruded into the northern phyllite and acted as a retaining wall, which prevented the deep phyllite from sliding towards the collapse pit. Under the combined influence of mining disturbance, rock mass creep, and the pushing of phyllite at the back of the branched orebody, the part of the branched orebody near the surface gradually undermined and eventually failed. It brought about cracking and toppling in the phyllite slope.

3.6. *Analysis of the Mechanism of Slope Failure.* Figure 22 shows the failure mechanism of the eastern slope as follows:

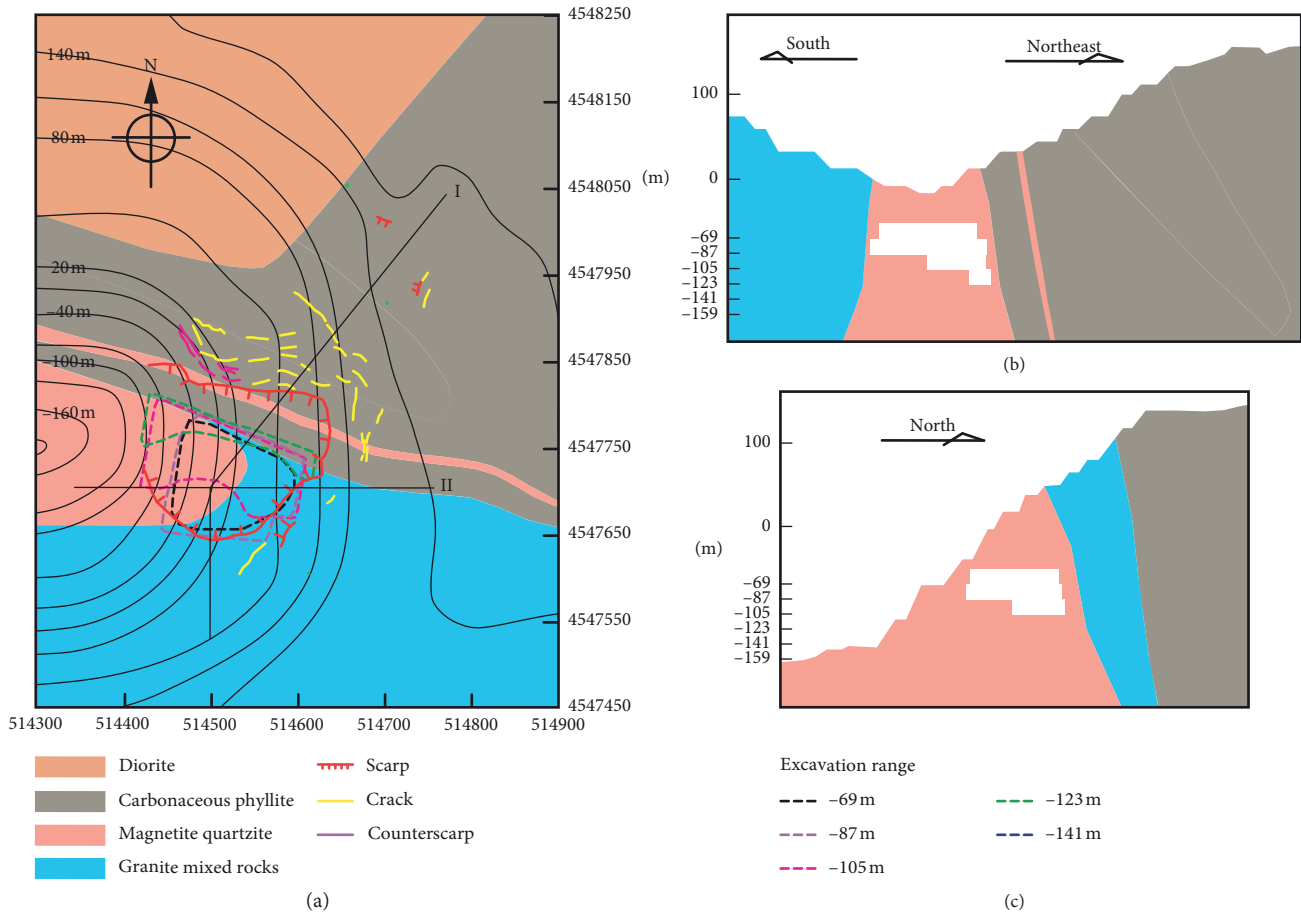


FIGURE 12: The engineering geomorphological map and mining progress on February 20, 2016. (a) Distribution of ground destruction. (b) At profile I. (c) At profile II.

- (a) The collapse of the rock stratum above the goaf caused by underground mining propagates upward to the surface to form a collapse pit.
- (b) With the development of mining, the cantilever beam structure of the rock mass gradually collapses, and the region of the surface subsidence is constantly expanded. The previous small landslide occurred when the rock mass, separated by open cracks around the collapse pit, slid into the pit.
- (c) There is a special mechanics structure on the northern slope, in which the wall-like branched orebody inserted into the phyllite is similar to a retaining wall. This structure prevents the collapse from propagating north further. However, due to the disturbance caused by continuous mining and the creep characteristics of phyllite, the superficial phyllite has a tendency to slide and topple. The expansion of the underground mining range and depth causes constant disturbance to the slope. The phyllite rock blocks cut by tension cracks begin to bend and topple into the collapse pit, and the range of cracking and toppling is constantly expanding. At the same time, the potential sliding surface of the shallow phyllite is continuously developed, which

extends to the northeast and produces shear failure away from the collapse pit.

- (d) Under the comprehensive influence of continuous underground mining disturbance, creep deformation of rock mass, and pushing of phyllite, the branch orebody is damaged. This means that the retaining wall near the surface fails. The phyllite moves downward along the potential sliding surface, resulting in a large landslide.

#### 4. Numerical Simulations

4.1. A Brief Introduction to RFPA3D. The RFPA3D model is based on the following assumptions:

- (1) The rock mass is assumed to be elastic-brittle with a residual strength at the elemental scale. The mechanical behavior of the rock is subject to an elastic damage constitutive law. The residual strain/deformation of the rock mass under unloading is not considered.
- (2) If the minimum stress of an element exceeds the tensile strength, the element is considered to fail in the tensile mode. When the shear stress of an

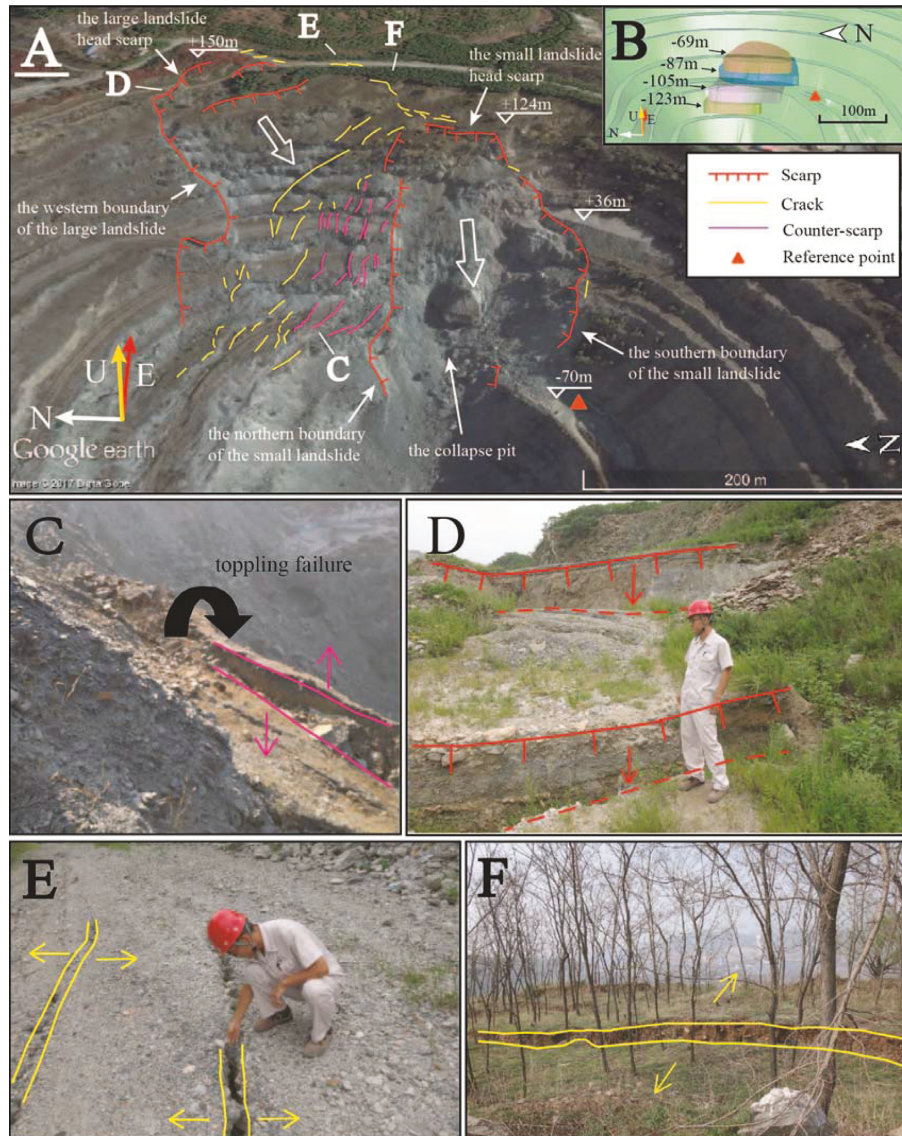


FIGURE 13: The survey of geomorphological changes of the eastern slope of the Yanqianshan Iron Mine (October 2016). (a) 3D view from Google Earth (17/10/2016). (b) The location of the mining area, which is observed through the same viewing angle as that of the Google Earth image (October 2016). (c) Counterscarps showing rock toppling failures on the phyllite slope. (d) Scarps away from the small landslide. (e, f) Tension cracks along the eastern boundary of the large landslide.

element satisfies the Mohr–Coulomb failure criterion, it is considered to fail in the shear mode.

- (3) The mechanical properties of the heterogeneity of the rock materials, including Young's modulus and the strength properties, conform to the Weibull distribution.

It is well known that acoustic emission (AE), generated by rapid microcrack growth, is a particular phenomenon correlated with the release of elastic energy produced by brittle fracture within the deformation of brittle materials. It provided abundant information in relation to the failure process in heterogeneous brittle rock. Monitoring AE or microseismic events generated during brittle material deformation is an effective way to detect the origination and the evolution of cracks [46, 47]. In engineering cases, such as

underground mining and landslides, AE or microseismic events are good indicators for assessing rock mass failure. A single AE event representing a microcracking event can indirectly estimate the damage evolution. Therefore, the AE counts are accounted for by the number of damaged elements, and changes in the number of AE events can reflect the degree of material destruction.

**4.2. Numerical Modeling.** Because of the imperfection of the preprocessing function of RFPA3D, a modeling method presented by Hu et al. is adopted to build a more accurate geological numerical model. Figure 23 shows the modeling process. First, the specialized mining software package SURPAC is used to establish a geological solid model, and then the solid model is discretized into a block model

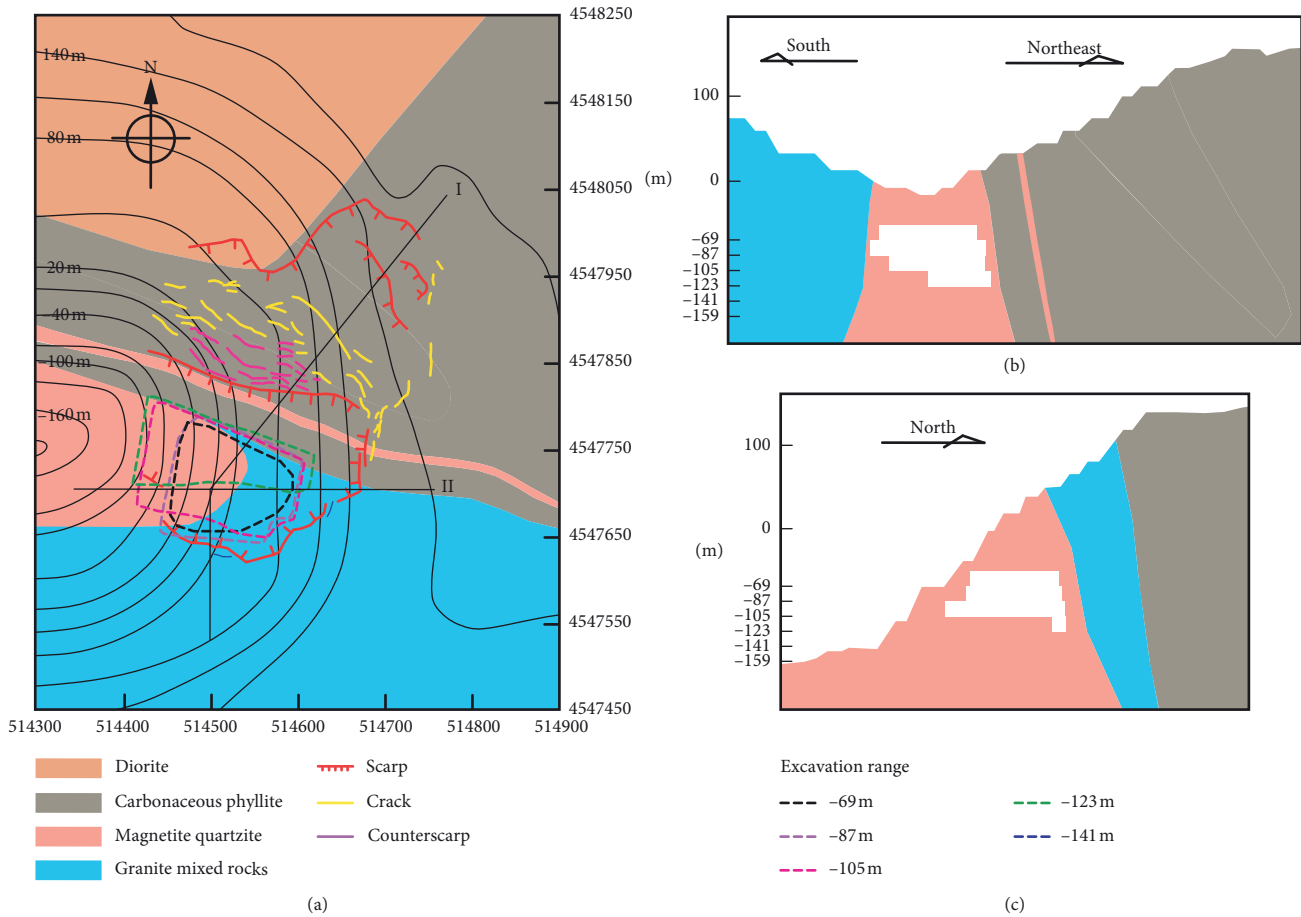


FIGURE 14: The engineering geomorphological map and mining progress on October 17, 2016. (a) Distribution of ground destruction. (b) At profile I. (c) At profile II.

composed of hexahedral elements. Subsequently, the information of the block model is dealt with by the conversion code named stor.m programmed in MATLAB to generate data files that can be read by RFPA3D. Finally, the data files are imported to the RFPA3D code to build the RFPA3D calculate model.

Based on the location and boundary of the mining area and the open pit, it is determined that a reasonable numerical simulation research area is 1.5 to 2 times the size of the largest mining area. As shown in Figure 1, the region is 900 m in the east-west direction, 1100 m in the north-south direction, and approximately 500 m in the vertical direction. The model contains four types of rock masses, including orebody, phyllite, mixed granite, and diorite. The macro-mechanical parameters of the rock masses are listed in Table 2.

The model consists of 8,97,471 hexahedral elements and 9,40,713 nodes. The side boundaries of the calculation domain are restrained in the normal direction, the bottom boundary is fixed, and the surface is free. The creep calculation method [41] was used to simulate the failure of the eastern slope. In the simulation, orebodies in three mining zones are mined to simulate the mining activities that took place from 2013 to 2017 in three stages of mining excavation, i.e., 2013~March 2014, March 2014~February 2016, and

February 2016~December 2017. The three stages of mining excavation were arranged successively at Step 2, Step 40, and Step 80.

4.3. Numerical Results. Figures 24 and 25 present the compressive and tensile stress evolution of the rock mass; the corresponding deformation displacements in the z-direction of the rock mass are shown in Figure 26.

After the first stage of mining excavation (2013~March 2014), the associated stress field in the rock mass was redistributed under the combined influence of the mining excavation and gravity loading. The high tension stress concentration, corresponding to the green part in the tensile stress evolution in Figure 25(a), occurred in the overlying rock of the mined-out area. At the same time, there was ground surface subsidence on the slope (Figure 26(a)).

The tensile stress along the surface projection boundary of the goaf grew constantly, and finally, the surface rock mass cracked under tensile force (Figures 24(b) and 25(b)). Then, the open crack continued to track the development of the tensile stress concentration area until the surface rock mass collapsed (Figures 24(c) and 25(c)).

After the second stage of mining excavation (March 2014~February 2016), the rock mass around the collapse pit

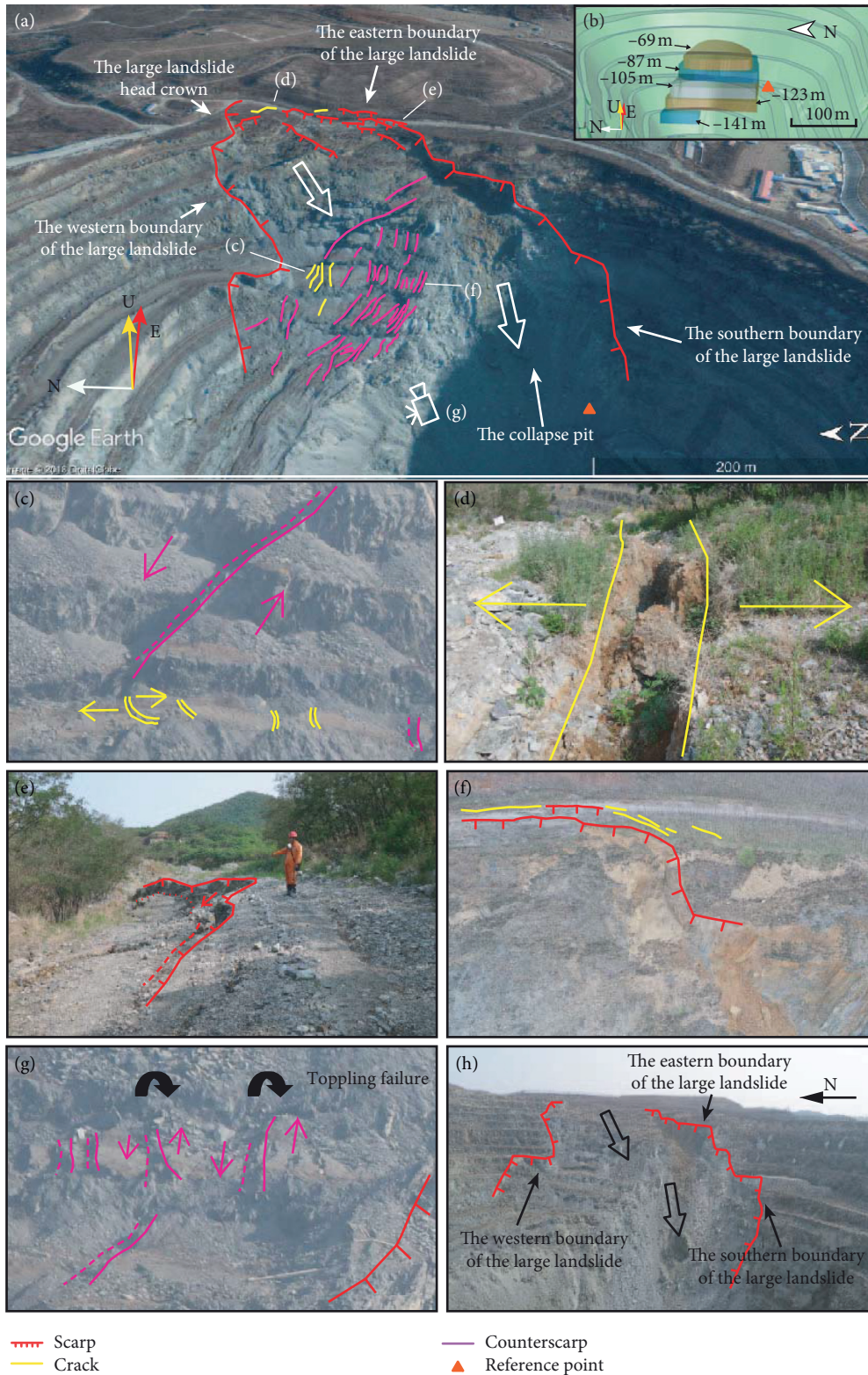


FIGURE 15: Survey of geomorphological changes of the eastern slope of the Yanqianshan Iron Mine (December 2017). (a) 3D view from Google Earth (27/12/2017). (b) The location of the mining area, which is observed through the same viewing angle as that of the Google Earth image (December 2017). (c) Tension cracks north of the counterscarps. (d) Tension cracks near the large landslide head crown (August 2017). (e, f) The eastern boundary of the large landslide (August 2017, October 2017). (g) Counterscarps behind the northern boundary of the small landslide. (h) The large landslide (view east).

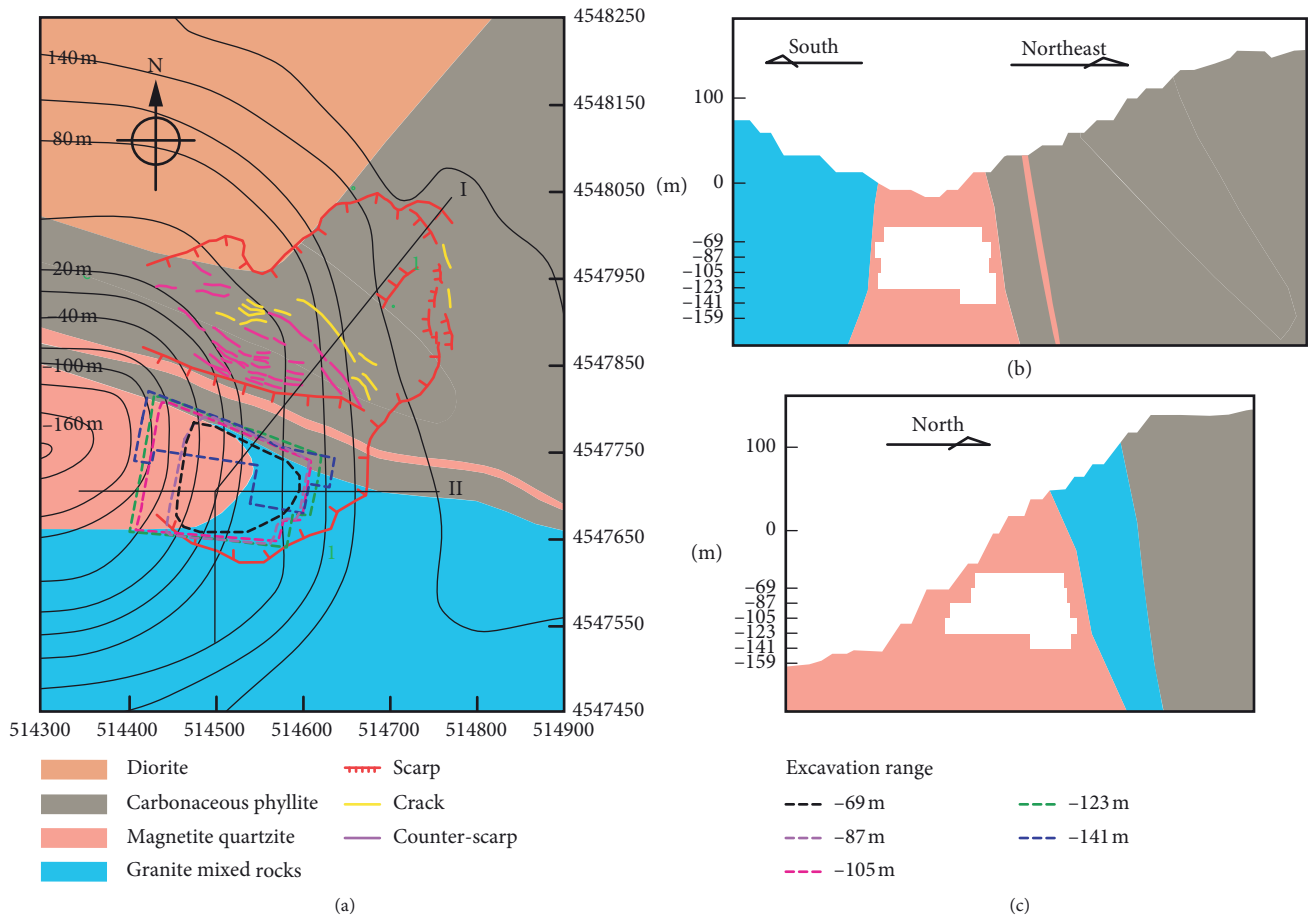


FIGURE 16: The engineering geomorphological map and mining progress on December 27, 2017. (a) Distribution of ground destruction. (b) At profile I. (c) At profile II.

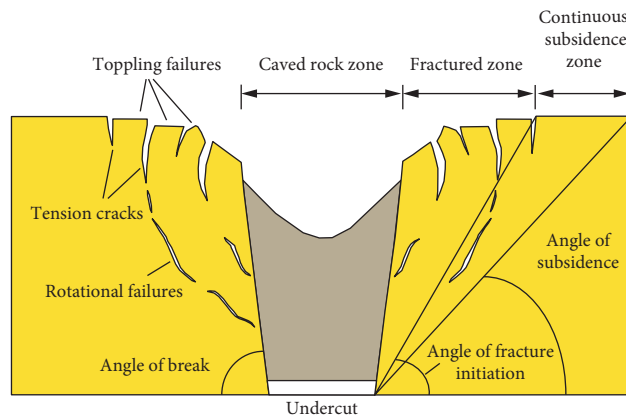


FIGURE 17: Conceptual representation of surface subsidence associated with block caving mining, subsidence characterization terminology, according to Van As [43].

rolled and slipped into the pit with the mined-out area enlarging, and the collapse pit expanded outwards (Figures 24(d), 24(e), 25(d), and 25(e)).

After the third stage of mining excavation (February 2016~December 2017), cracks appeared between the phyllite and diorite rock mass on the northern slope, and these cracks eventually developed to form a continuous

fracture zone. On the contrary, due to creep deformation, the engineering quality of rock masses continually declined. Finally, under the action of gravity, a slip surface of the phyllite slope was formed by shear slip, and the phyllite rock mass, which was separated by the fracture zone and the slip surface, slid southwestward (Figures 24(f) and 25(f)).

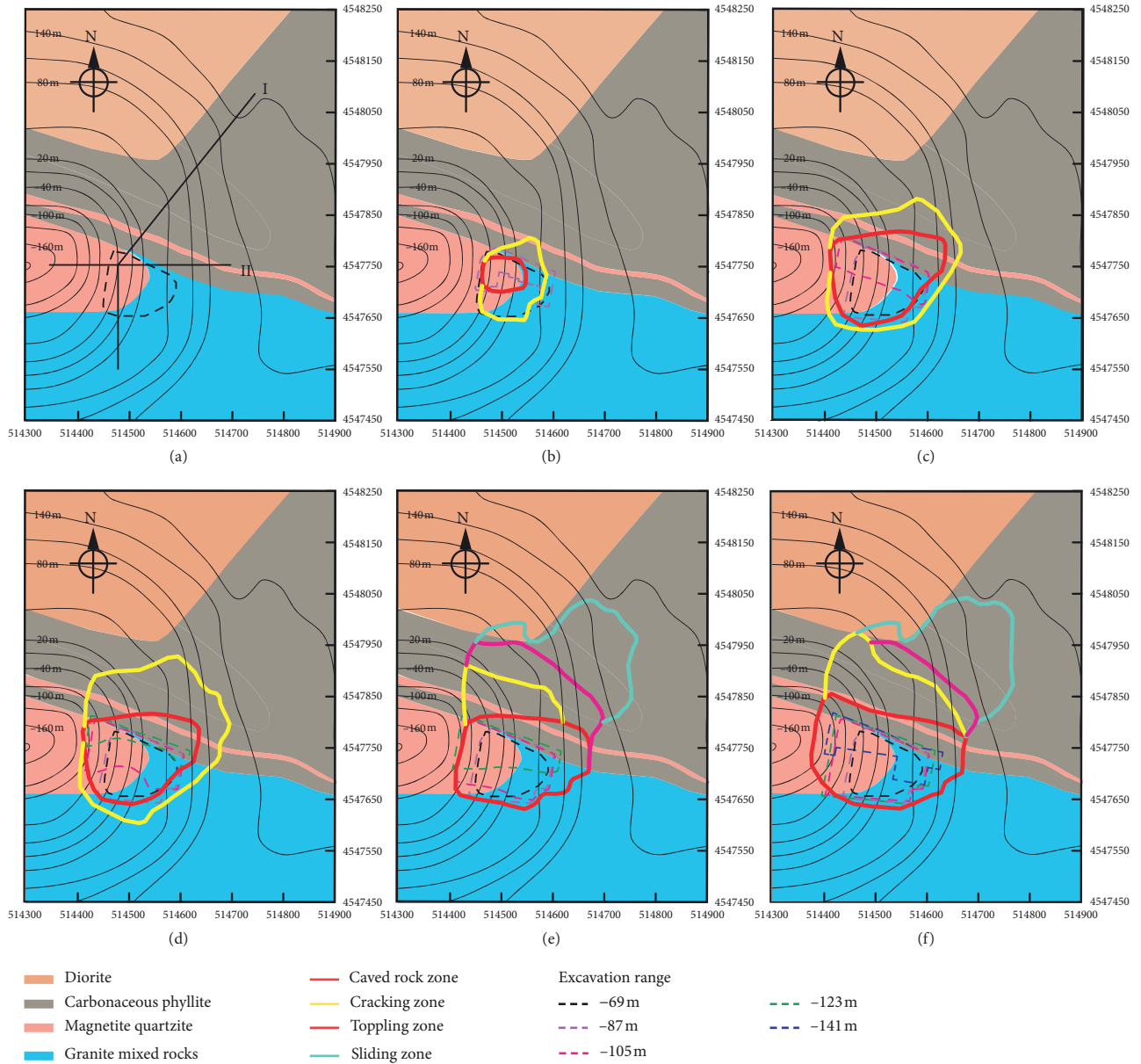


FIGURE 18: The variation of the surface failure partition on the eastern slope of the Yanqianshan Iron Mine.

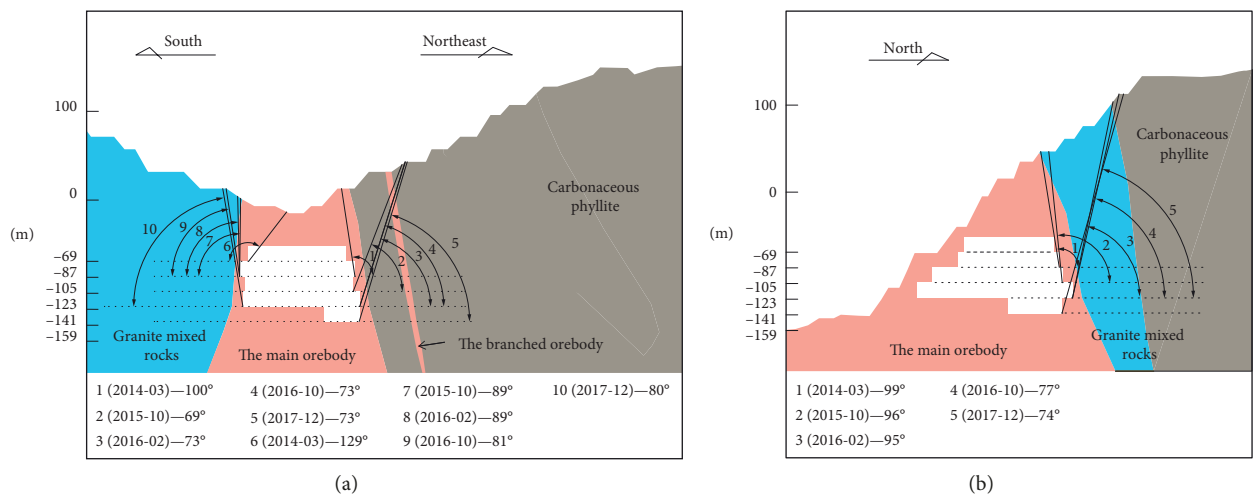


FIGURE 19: The change of break angles of five periods. (a) At profile I. (b) At profile II.

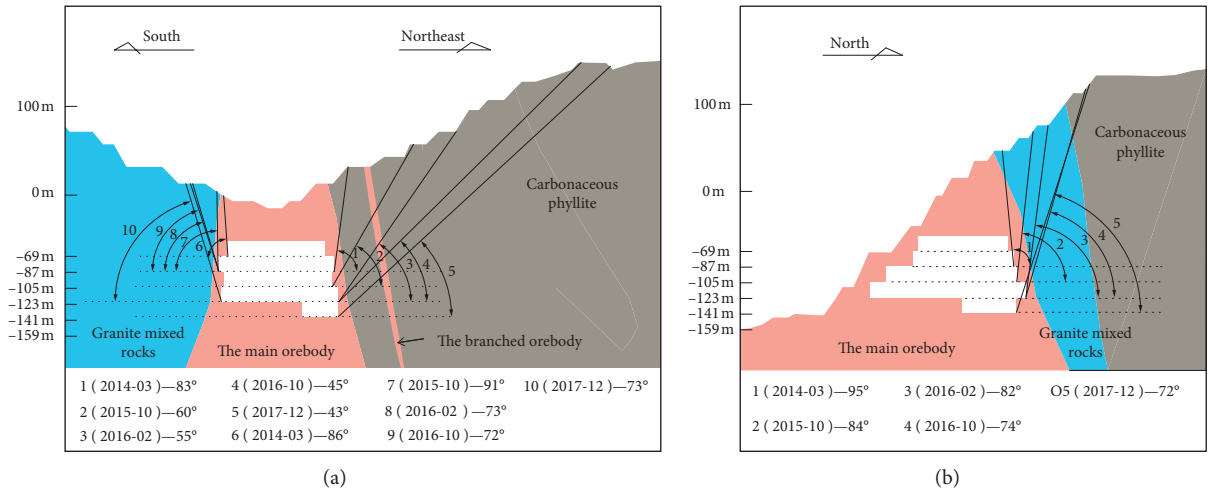


FIGURE 20: The change in fracture initiation angles over five periods. (a) At profile I. (b) At profile II.

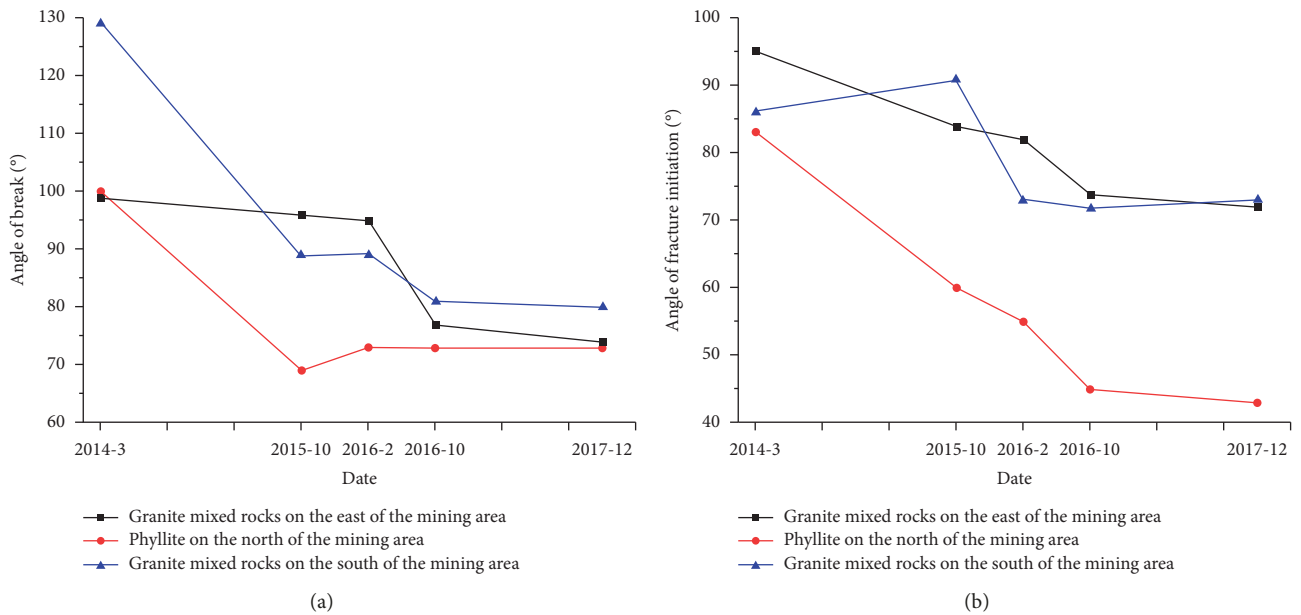


FIGURE 21: The change rule of (a) the break angle and (b) the fracture initiation angle.

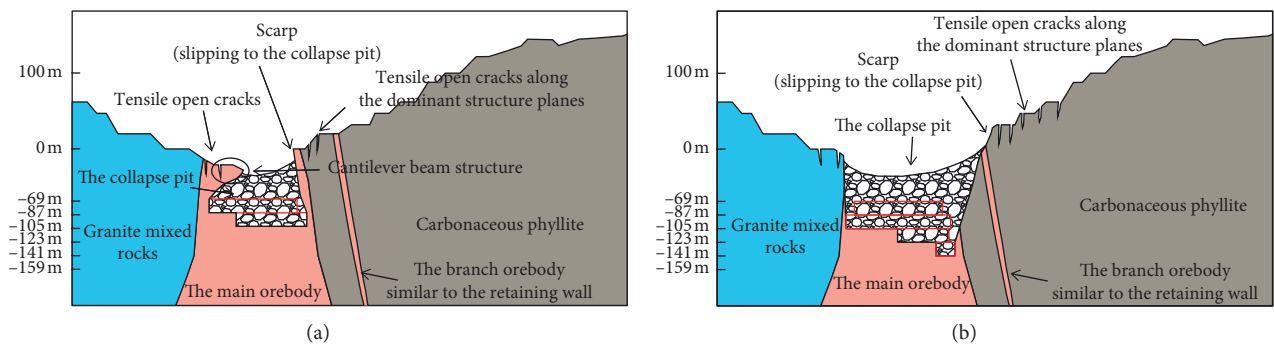


FIGURE 22: Continued.

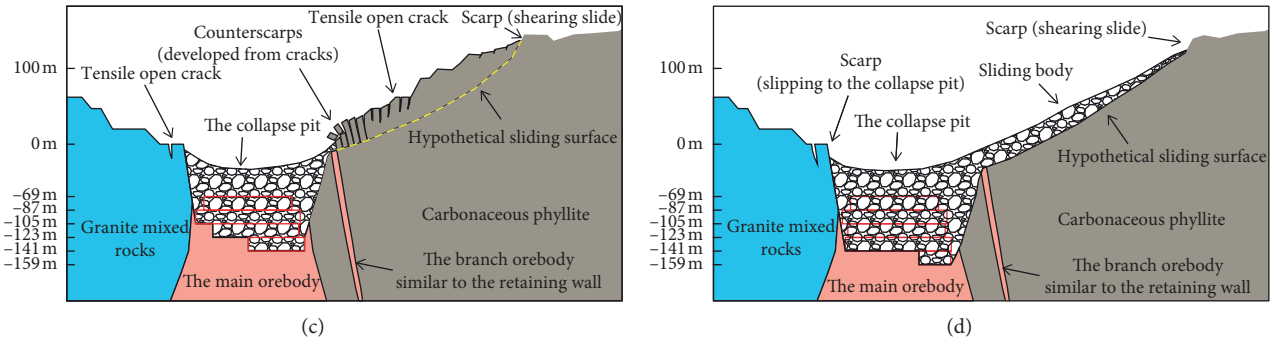


FIGURE 22: An illustration of the failure mechanism of the eastern slope.

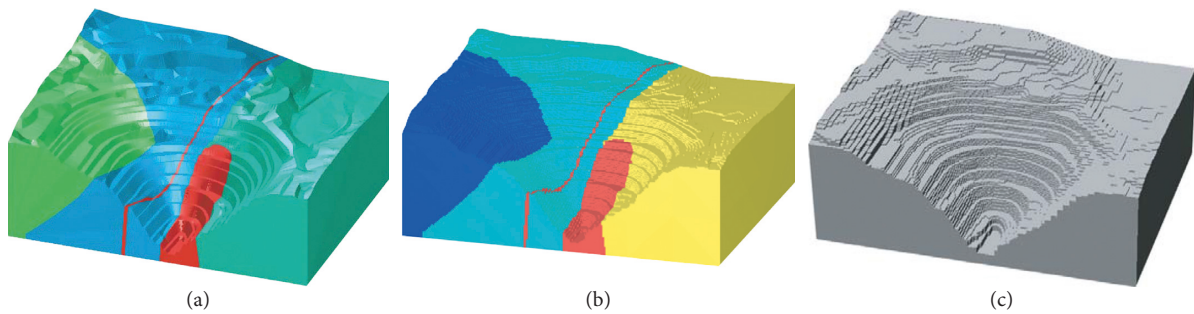


FIGURE 23: The modeling process. (a) The solid model in SURPAC, (b) the block model in SURPAC, and (c) the RFP3D model.

TABLE 2: The macromechanical parameters of the rock masses.

Rock formation	Location	Heterogeneity index (m)	Uniaxial compressive strength (MPa)	Young's modulus (GPa)	Poisson's ratio	Internal friction angle (°)	Density (g/cm <sup>3</sup> )
Orebody	Middle	7	94.5	27.9	0.14	14.6	3.4
Mixed granite	South	7	57.0	6.7	0.2	33.8	2.7
Phyllite	North	7	28.2	5.3	0.21	32	2.6
Diorite	North	7	75.5	11.5	0.2	34.9	2.8

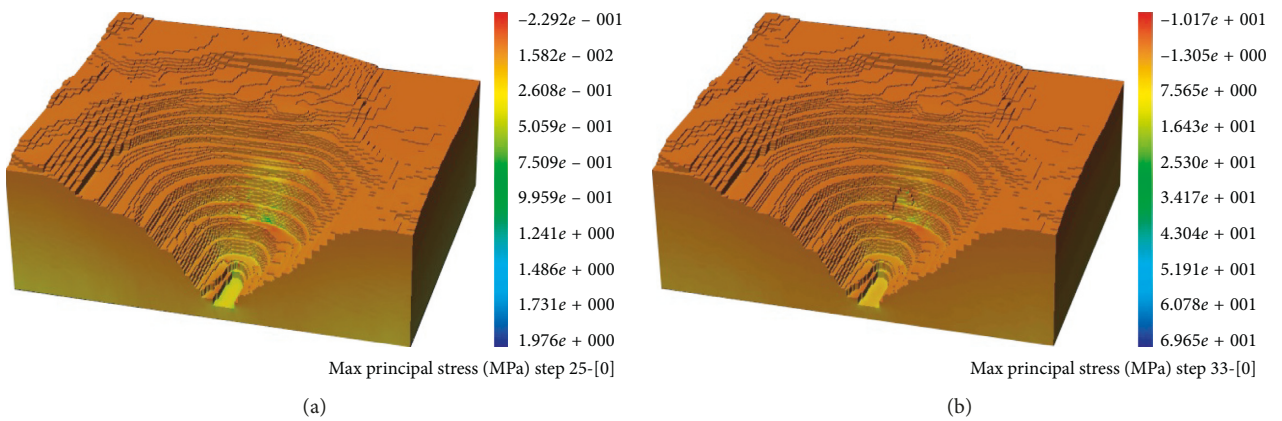


FIGURE 24: Continued.

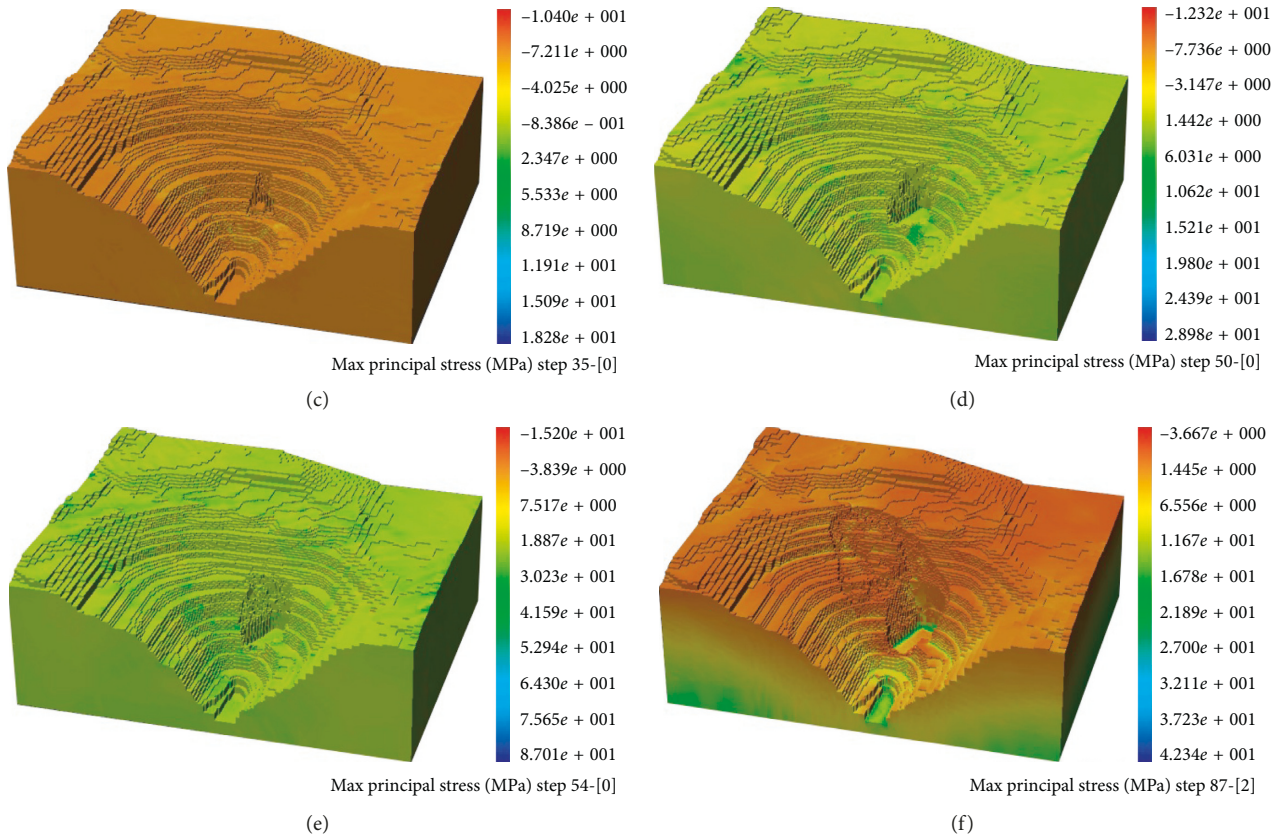


FIGURE 24: The associated compressive stress evolution of the rock mass with mining excavation.

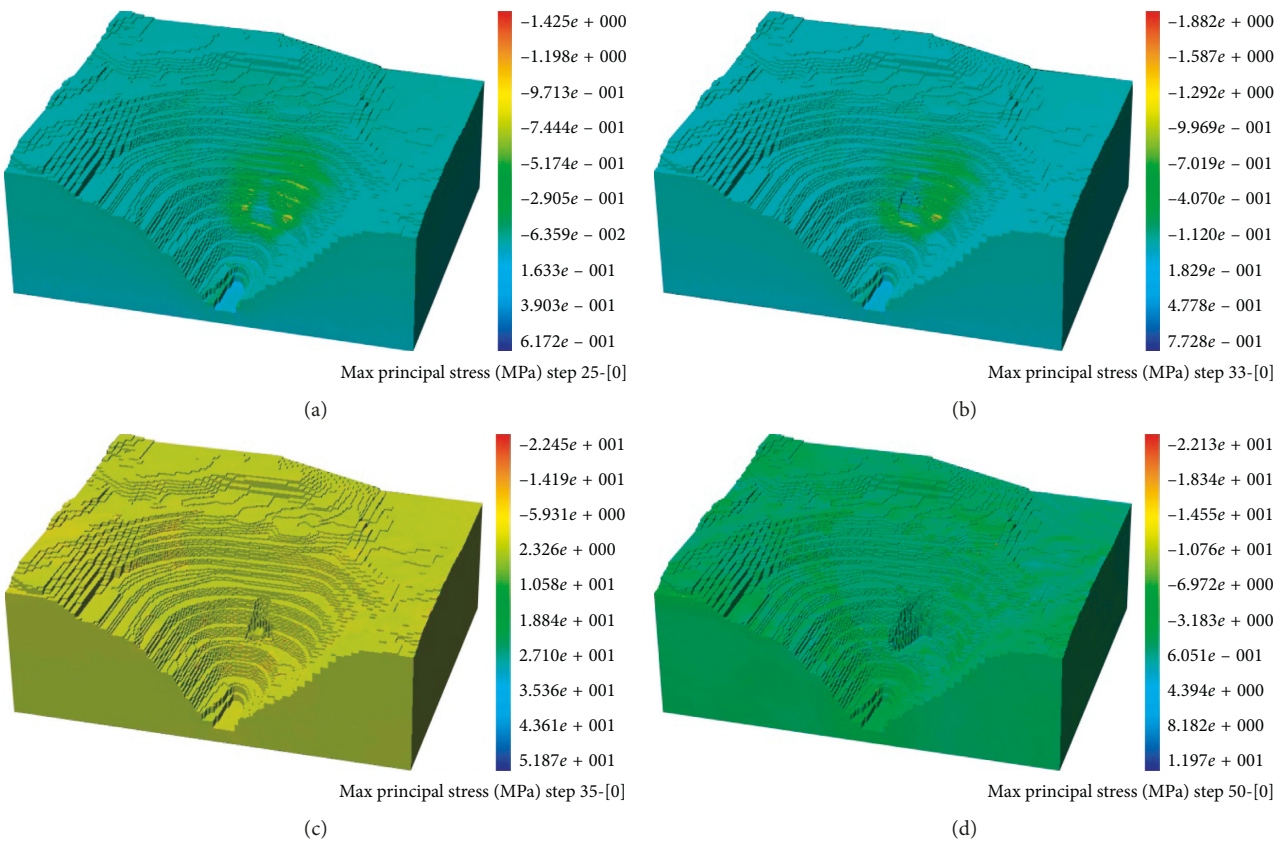


FIGURE 25: Continued.

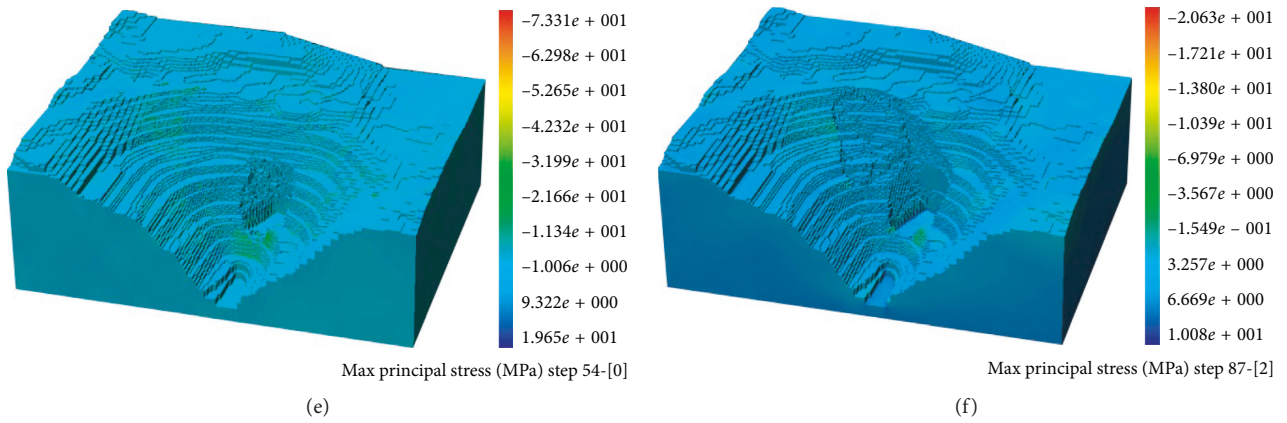


FIGURE 25: The associated tensile stress evolution of the rock mass with mining excavation.

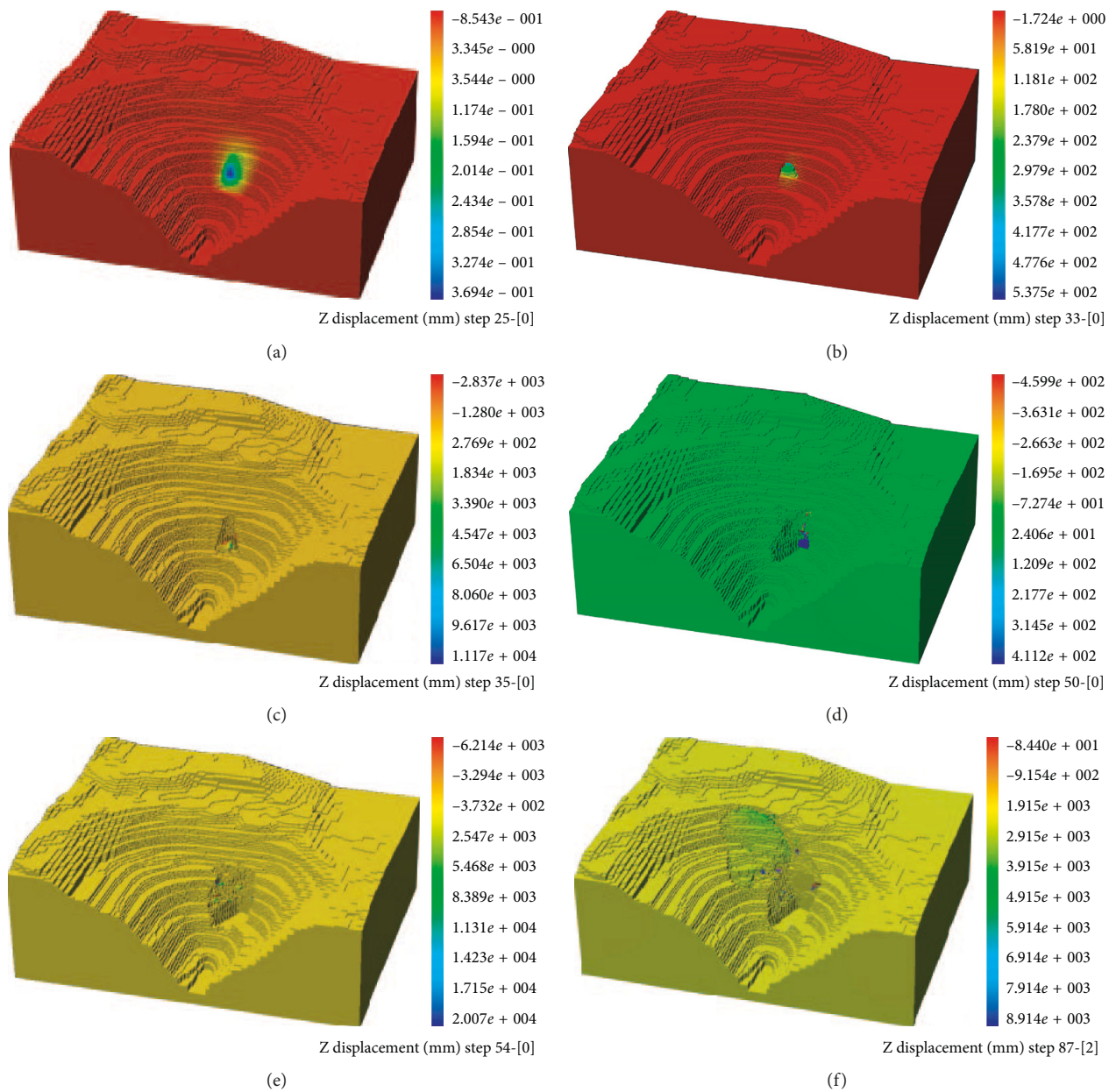


FIGURE 26: The associated deformation displacement in the z-direction of the rock mass with mining excavation.

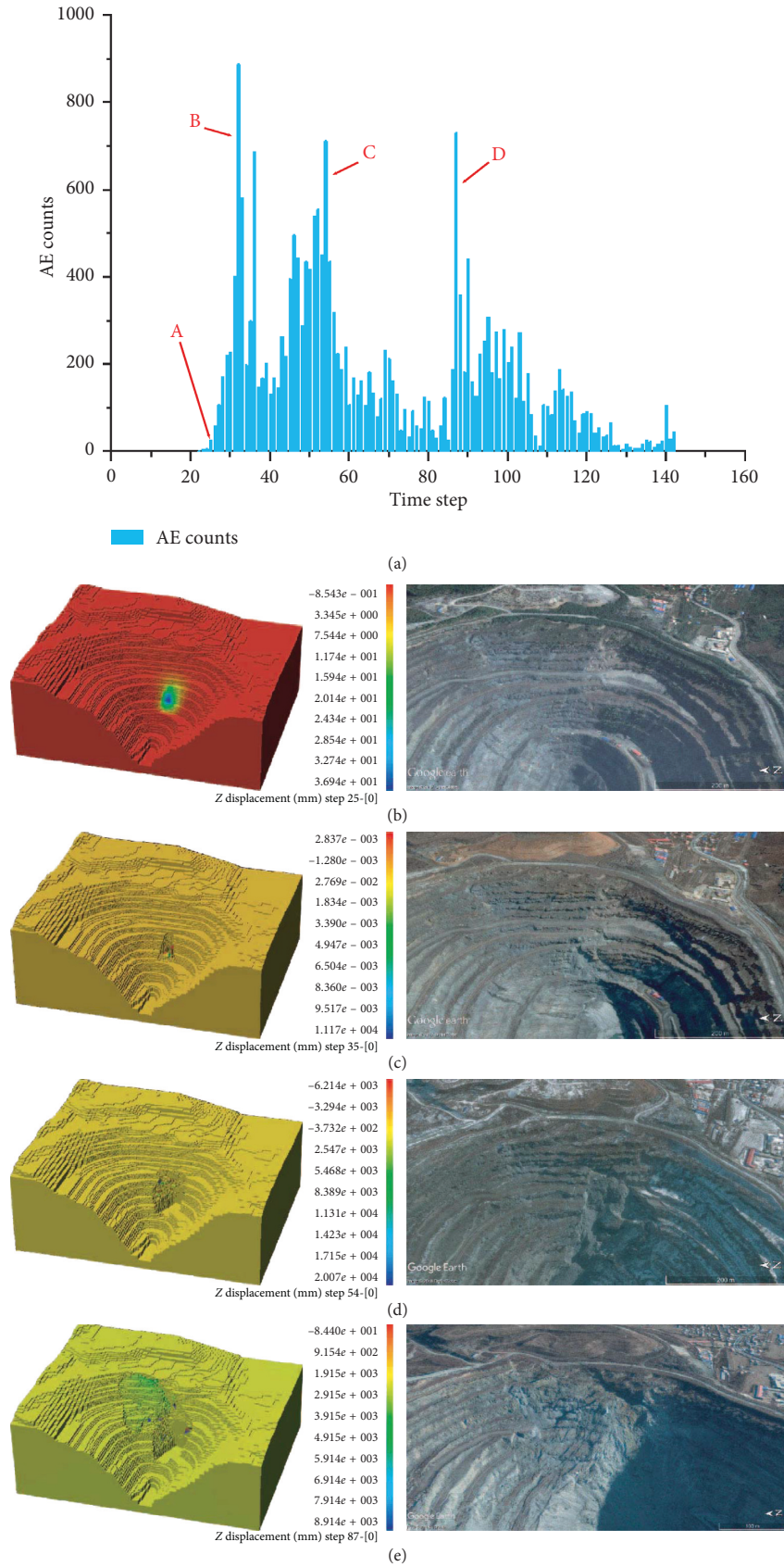


FIGURE 27: Simulated AE events with mining excavation.

The simulated failure pattern is in good agreement with the observed in situ sliding failure pattern, as shown in Figure 26. Figure 27 shows the numerically simulated AE events or associated damage event count sequences during mining. It can be shown that there are three peak periods of AE events, respectively, in steps 32~36, 50~54, and 87~90. Each peak corresponds to the large-scale destruction after each excavation, which proves the driving effect of the excavation under the slope on the failure of the slope and verifies the reliability of the numerical simulation.

## 5. Conclusions

In this paper, Google Earth images and field investigations were used to analyze the process of fracture propagation on the eastern slope under the influence of underground mining. Based on the site investigations, the failure mechanism and the damage process of the eastern slope were investigated by numerical models. According to the above comprehensive research method, the following conclusions can be obtained:

- (1) The combined survey method of Google Earth and field investigations can effectively implement long-term and low-cost monitoring of surface deformation.
- (2) Three typical characteristics of surface deformation were found in the failure process of the eastern slope of the Yanqianshan Iron Mine: open cracks, scarps, and counterscarps. Open cracks, developed along the existing dominant structure planes, were mainly distributed on the phyllite slope north of the mining area. The open cracks divided the phyllite rock mass into discrete subvertical layered rocks. With layered rocks bending and toppling, open cracks developed into counterscarps. Scarps are divided into two categories: some around the mining area caused by ground collapse and the others far away from the collapsed open pit caused by massive rock mass sliding.
- (3) The process of eastern slope failure can be divided into three stages. In the first stage, roof failure of the mined-out area brought about surface collapse. In the second, it resulted in a small landslide in which the rock mass around the collapse pit slid and fell into the open pit. Finally, mining disturbance and creep deformation of the phyllite slope caused a large landslide on the northern phyllite slope.
- (4) Based on the characteristics of ground deformation, the destruction area of the eastern slope can be divided into four zones: caved rock area, cracking zone, toppling zone, and sliding zone. Combined with the analysis of break and fracture initiation angles, it is shown that the wall-like branched orebody, which is inserted into phyllite, acts as a retaining wall in the transition stage from the early small landslide to the final large landslide. After the collapse pit was formed, the wall-like orebody restricted the

southward displacement of phyllite to the north of the mining area. With the disturbance of underground mining and the pushing of the potential sliding body on the northern phyllite slope, the retaining wall-like structure gradually trended towards instability. It resulted in a dynamic and cyclic change pattern of geomorphic destruction features on the phyllite slope: first, open cracks were formed; then, the existing open cracks developed into counterscarps; finally, new open cracks were generated which could become new counterscarps.

- (5) The location and scope of the previous small landslide were controlled by the mined-out area. The location and scope of the later large landslide were controlled by the contact fault between the diorite and phyllite, the dominant joint sets of the phyllite, and the potential sliding surface.
- (6) RFPA3D is used to simulate the process of slope failure with underground mining. The stress analysis reveals that the slope failure is mainly caused by tensile failure and shear slip. Displacement analysis and AE event statistics establish three stages of slope failure: collapse, a small landslide caused by the collapse, and a large landslide on the northern phyllite slope. The simulation results are consistent with the field observations.

## Data Availability

The data used to support the findings of this study are available from the corresponding author upon request.

## Conflicts of Interest

The authors declare that they have no conflicts of interest.

## Acknowledgments

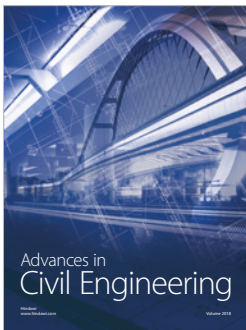
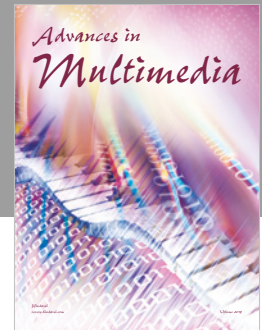
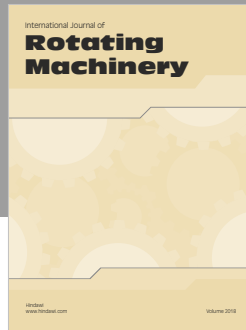
The authors would like to thank the financial support provided by the National Key Research and Development Program of China (Grant no. 2016YFC0801601) and the National Natural Science Foundation of China (Grant no. 51534003).

## References

- [1] M. I. Álvarez-Fernández, C. González-Nicieza, A. Menéndez-Díaz, and A. E. Álvarez-Vigil, "Generalization of the n-k influence function to predict mining subsidence," *Engineering Geology*, vol. 80, no. 1-2, pp. 1-36, 2005.
- [2] L. Yi and J. W. Cheng, "An influence function method based subsidence prediction program for longwall mining operations in inclined coal seams," *Mining Science & Technology*, vol. 19, no. 5, pp. 592-598, 2009.
- [3] K. Xia, C. Chen, H. Fu, Y. Pan, and Y. Deng, "Mining-induced ground deformation in tectonic stress metal mines: a case study," *Engineering Geology*, vol. 210, no. 3, pp. 212-230, 2016.
- [4] H. Zahiri, D. R. Palamara, P. Flentje, G. M. Brassington, and E. Baafi, "A GIS-based Weights-of-Evidence model for

- mapping cliff instabilities associated with mine subsidence," *Environmental Geology*, vol. 51, no. 3, pp. 377–386, 2006.
- [5] M. Marschalko, I. Yilmaz, M. Bednárík, and K. Kubečka, "Influence of underground mining activities on the slope deformation genesis: Doubrava Vrchovec, Doubrava Ujala and Staric case studies from Czech Republic," *Engineering Geology*, vol. 147–148, no. 15, pp. 37–51, 2012.
- [6] E. F. Salmi, M. Nazem, and M. Karakus, "Numerical analysis of a large landslide induced by coal mining subsidence," *Engineering Geology*, vol. 217, pp. 141–152, 2017.
- [7] F. Sousa, S. O. Akciz, J. C. Harvey et al., *Field and LiDAR Observations of the Hector Mine California 1999 Surface Rupture*, AGU Fall Meeting, San Francisco, CA, USA, 2014.
- [8] R. A. Kromer, D. J. Hutchinson, M. J. Lato, D. Gauthier, and T. Edwards, "Identifying rock slope failure precursors using LiDAR for transportation corridor hazard management," *Engineering Geology*, vol. 195, pp. 93–103, 2015.
- [9] A. Laribi, J. Walstra, M. Ougrine, A. Seridi, and N. Dechemi, "Use of digital photogrammetry for the study of unstable slopes in urban areas: case study of the El Biar landslide, Algiers," *Engineering Geology*, vol. 187, pp. 73–83, 2015.
- [10] A. Jarosz and D. Wanke, "Use of InSAR for monitoring of mining deformations," in *Proceedings of Fringe Workshop*, p. 550, Frascati, Italy, December 2003.
- [11] G. Herrera, R. Tomás, F. Vicente, J. M. Lopez-Sanchez, J. J. Mallorquí, and J. Mulas, "Mapping ground movements in open pit mining areas using differential SAR interferometry," *International Journal of Rock Mechanics and Mining Sciences*, vol. 47, no. 7, pp. 1114–1125, 2010.
- [12] F. Bozzano, I. Cipriani, P. Mazzanti, and A. Prestininzi, "Displacement patterns of a landslide affected by human activities: insights from ground-based InSAR monitoring," *Natural Hazards*, vol. 59, no. 3, pp. 1377–1396, 2011.
- [13] A. Clayton, D. Stead, D. Kinakin, and A. Wolter, "Engineering geomorphological interpretation of the Mitchell Creek landslide, British Columbia, Canada," *Landslides*, vol. 14, no. 5, pp. 1655–1675, 2017.
- [14] R. M. Hetherington, *Slope stability analysis of Mount Meager, south-western British Columbia, Canada*, Dissertations & Theses-Gradworks, Michigan Technological University, Houghton, MI, USA, 2014.
- [15] F. G. Murillo-García et al., "Satellite stereoscopic pair images of very high resolution: a step forward for the development of landslide inventories," *Landslides*, vol. 12, no. 2, p. 293, 2015.
- [16] M. Yu et al., "Application of virtual earth in 3D terrain modeling to visual analysis of large-scale geological disasters in mountainous areas," *Environmental Earth Sciences*, vol. 75, no. 7, pp. 1–7, 2016.
- [17] T. Villegas, E. Nordlund, and C. Dahnér-Lindqvist, "Hang-ingwall surface subsidence at the Kiirunavaara mine, Sweden," *Engineering Geology*, vol. 121, no. 1–2, pp. 18–27, 2011.
- [18] N. E. Yasitli and B. Unver, "3D numerical modeling of longwall mining with top-coal caving," *International Journal of Rock Mechanics and Mining Sciences*, vol. 42, no. 2, pp. 219–235, 2005.
- [19] B. Unver and N. E. Yasitli, "Modelling of strata movement with a special reference to caving mechanism in thick seam coal mining," *International Journal of Coal Geology*, vol. 66, no. 4, pp. 227–252, 2006.
- [20] R. Singh, P. K. Mandal, A. K. Singh, R. Kumar, J. Maiti, and A. K. Ghosh, "Upshot of strata movement during underground mining of a thick coal seam below hilly terrain," *International Journal of Rock Mechanics and Mining Sciences*, vol. 45, no. 1, pp. 29–46, 2008.
- [21] M. R. Islam, D. Hayashi, and A. B. M. Kamruzzaman, "Finite element modeling of stress distributions and problems for multi-slice longwall mining in Bangladesh, with special reference to the Barapukuria coal mine," *International Journal of Coal Geology*, vol. 78, no. 2, pp. 91–109, 2009.
- [22] P. R. Helm, C. T. Davie, and S. Glendinning, "Numerical modelling of shallow abandoned mine working subsidence affecting transport infrastructure," *Engineering Geology*, vol. 154, no. 154, pp. 6–19, 2013.
- [23] X. Li, D. Li, Z. Liu, G. Zhao, and W. Wang, "Determination of the minimum thickness of crown pillar for safe exploitation of a subsea gold mine based on numerical modelling," *International Journal of Rock Mechanics and Mining Sciences*, vol. 57, no. 1, pp. 42–56, 2013.
- [24] N. Xu, P. H. S. W. Kulatilake, H. Tian, X. Wu, Y. Nan, and T. Wei, "Surface subsidence prediction for the WUTONG mine using a 3-D finite difference method," *Computers and Geotechnics*, vol. 48, no. 3, pp. 134–145, 2013.
- [25] Y. Chen, Q. Cai, T. Shang, H. Peng, W. Zhou, and S. Chen, "Zonal extraction technology and numerical simulation analysis in open pit coal mine," *International Journal of Mining Science and Technology*, vol. 22, no. 4, pp. 487–491, 2012.
- [26] W. Yang and X. Xia, "Prediction of mining subsidence under thin bedrocks and thick unconsolidated layers based on field measurement and artificial neural networks," *Computers & Geosciences*, vol. 52, no. 1, pp. 199–203, 2013.
- [27] Z. Zhang, M. Zhang, and Q. Zhao, "A simplified analysis for deformation behavior of buried pipelines considering disturbance effects of underground excavation in soft clays," *Arabian Journal of Geosciences*, vol. 8, no. 10, pp. 7771–7785, 2015.
- [28] G. S. P. Singh and U. K. Singh, "A numerical modeling approach for assessment of progressive caving of strata and performance of hydraulic powered support in longwall workings," *Computers and Geotechnics*, vol. 36, no. 7, pp. 1142–1156, 2009.
- [29] A. Vyazmensky, D. Stead, D. Elmo, and A. Moss, "Numerical analysis of block caving-induced instability in large open pit slopes: a finite element/discrete element approach," *Rock Mechanics and Rock Engineering*, vol. 43, no. 1, pp. 21–39, 2010.
- [30] M. Shabanimashcool and C. C. Li, "Numerical modelling of longwall mining and stability analysis of the gates in a coal mine," *International Journal of Rock Mechanics and Mining Sciences*, vol. 51, no. 4, pp. 24–34, 2012.
- [31] F. Gao, D. Stead, and J. Coggan, "Evaluation of coal longwall caving characteristics using an innovative UDEC Trigon approach," *Computers and Geotechnics*, vol. 55, no. 55, pp. 448–460, 2014.
- [32] A. Lisjak, D. Figi, and G. Grasselli, "Fracture development around deep underground excavations: Insights from FDEM modelling," *Journal of Rock Mechanics and Geotechnical Engineering*, vol. 6, no. 6, pp. 493–505, 2014.
- [33] F. Wang, C. Zhang, X. Zhang, and Q. Song, "Overlying strata movement rules and safety mining technology for the shallow depth seam proximity beneath a room mining goaf," *International Journal of Mining Science and Technology*, vol. 25, no. 1, pp. 139–143, 2015.
- [34] R. Gu and U. Ozbay, "Numerical investigation of unstable rock failure in underground mining condition," *Computers and Geotechnics*, vol. 63, no. 63, pp. 171–182, 2015.
- [35] M. Svartsjaern, D. Saiang, E. Nordlund, and A. Eitzenberger, "Conceptual numerical modeling of large-scale footwall

- behavior at the Kiirunavaara mine, and implications for deformation monitoring,” *Rock Mechanics & Rock Engineering*, vol. 49, no. 3, pp. 1–18, 2016.
- [36] N. Xu, J. Zhang, H. Tian, G. Mei, and Q. Ge, “Discrete element modeling of strata and surface movement induced by mining under open-pit final slope,” *International Journal of Rock Mechanics and Mining Sciences*, vol. 88, pp. 61–76, 2016.
- [37] L. C. Li, C. A. Tang, C. W. Li, and W. C. Zhu, “Slope stability analysis by SRM-based rock failure process analysis (RFPA),” *Geomechanics and Geoengineering*, vol. 1, no. 1, pp. 51–62, 2006.
- [38] C. A. Tang, H. Liu, P. K. K. Lee, Y. Tsui, and L. G. Tham, “Numerical studies of the influence of microstructure on rock failure in uniaxial compression—Part I: effect of heterogeneity,” *International Journal of Rock Mechanics and Mining Sciences*, vol. 37, no. 4, pp. 555–569, 2000.
- [39] C. A. Tang, L. G. Tham, P. K. K. Lee, Y. Tsui, and H. Liu, “Numerical studies of the influence of microstructure on rock failure in uniaxial compression - Part II: constraint, slenderness and size effect,” *International Journal of Rock Mechanics and Mining Sciences*, vol. 37, no. 4, pp. 571–583, 2000.
- [40] Z. Z. Liang, H. Xing, S. Y. Wang, D. J. Williams, and C. A. Tang, “A three-dimensional numerical investigation of the fracture of rock specimens containing a pre-existing surface flaw,” *Computers and Geotechnics*, vol. 45, no. 45, pp. 19–33, 2012.
- [41] T. Xu, Q. Xu, M. Deng, T. Ma, T. Yang, and C.-A. Tang, “A numerical analysis of rock creep-induced slide: a case study from Jiweishan Mountain, China,” *Environmental Earth Sciences*, vol. 72, no. 6, pp. 2111–2128, 2014.
- [42] F. Zhang, T. Yang, L. Li, Z. Wang, and P. Xiao, “Cooperative monitoring and numerical investigation on the stability of the south slope of the Fushun west open-pit mine,” *Bulletin of Engineering Geology & the Environment*, pp. 1–21, 2018.
- [43] A. Van As, “Subsidence definitions for block caving mines,” Technical Report, p. 59, Rio Tinto Technical Services, Sydney, Australia, 2003.
- [44] G. Manthei and J. Eisenblätter, *Acoustic Emission in Study of Rock Stability*, Springer, Berlin, Germany, 2008.
- [45] C. Tang and C. Tang, “Numerical simulation of progressive rock failure and associated seismicity,” *International Journal of Rock Mechanics and Mining Sciences*, vol. 34, no. 2, pp. 249–261, 1997.
- [46] H. U. Ying-Peng, R. Feng-yu, D. Hang-xing, and F. Yu, “RFPA-(3D) modeling and application for complex rock masses based on SURPAC,” *Journal of Northeastern University*, vol. 39, no. 7, 2018.
- [47] Surpac Minex Group, *SURPAC Version V5. 2-D*, Surpac Minex Group, Mainland Street Suite, Vancouver, Canada, 2006.



**Hindawi**

Submit your manuscripts at  
[www.hindawi.com](http://www.hindawi.com)

